JAERI-M
83-027

EVALUATION REPORT ON CCTF CORE-I REFLOOD TEST CI-5 (RUN 14)

—OVER-ALL SYSTEM THERMO-HYDRODYNAMIC BEHAVIORS OBSERVED IN THE BASE CASE TEST—

February 1983

Yoshio MURAO, Hajime AKIMOTO, Takashi SUDOH
and Tsutomu OKUBO

日本原子力研究所
Japan Atomic Energy Research Institute

JAERI-M レポートは，日本原子力研究所が不定期に公刊している研究報告書です。
入手の問合わせは，日本原子力研究所技術情報部情報資料課（〒319—11 茨城県那珂郡東海村）あて，お申しこしください。なお，このほかに財団法人原子力弘済会資料センター（〒319-11 茨城県那珂郡東海村日本原子力研究所内）で複写による実費頒布をおこなっております。

JAERI-M reports are issued irregularly.
Inquiries about availability of the reports should be addressed to Information Section, Division of Technical Information, Japan Atomic Energy Research Institute, Tokai-mura, Naka-gun, Ibaraki-ken 319-11, Japan.

編集兼発行　日本原子力研究所
印　　刷　山田軽印刷所

JAERI-M 83-027

Evaluation Report on CCTF Core-I Reflood Test C1-5 (Run 14)

— Over-all system thermo-hydrodynamic behaviors observed in the base case test —

Yoshio MURAO, Hajime AKIMOTO, Takashi SUDOH and Tsutomu OKUBO

Division of Nuclear Safety Research,
Tokai Research Establishment, JAERI

(Received January 29, 1983)

A study of a cylindrical core test facility (CCTF) test was performed for modeling the system behavior during the reflood phase of a PWR-LOCA and the following conclusions were obtained:

1) With the exception of some points, the observed phenomena are similar to a model derived from an evaluation model for a PWR safety evaluation.
2) The different points are the water accumulation in the upper plenum, the ECC bypass in the downcomer, the reduction of the effective downcomer head and the pressure drop at the broken cold leg nozzle and in the interconnected pipes.

Keywords: Reflood Experiment, Reactor Safety, Loss-of-coolant Accident, Heat Transfer, Two-phase Flow, PWR, Hydrodynamics

---

The work was performed under contract with the Atomic Energy Bureau of Science and Technology Agency of Japan.

JAERI—M 83—027

大型再冠水円筒第一次炉心試験C1－5（Run 14）評価報告書
— 基準試験におけるシステム全体の熱水力挙動 —

日本原子力研究所東海研究所安全工学部
村尾良夫・秋本　肇・須藤高史
大久保努

（1983年1月29日受理）

再浸水，再冠水現象の研究のために行った円筒炉心試験装置による試験結果を解析し，次の結論を得た。

1）　観測された現象は，いくつかの点を除き，PWR安全評価用の評価モデルに基づいて開発したモデルと同様のものである。

2）　異なる点は，上部プレナムの蓄水，ダウンカマ内のECCのバイパス，有効ダウンカマ水頭の低下および，破断コールドレグノズルおよび連結配管内の圧力損失である。

本報告書は，電源開発促進対策特別会計法に基づき，科学技術庁からの受託によって行った研究の成果である。

Contents

目　　次

List of tables

List of figures

I. Introduction

A series of reflood tests was conducted with JAERI's Cylindrical Core Test Facility (CCTF) since March, 1979. CCTF with its integral simulation of a PWR system and extensive measurement systems has already yielded a large amount of information on the overall thermo-hydrodynamic behavior and system effects during the reflood phase of a loss-of-coolant accident (LOCA) in a PWR.

The objectives of the CCTF tests are:

(1) Demonstration of the effectiveness of emergency core cooling system (ECCS) in a PWR during the refill and reflood phases of a LOCA.

(2) Provision of information for analytical modeling of thermo-hydrodynamic phenomena during the refill and reflood phases in a PWR-LOCA.

(3) Verification of a reflood analysis code, "REFLA", and a US-developed reactor transient analysis code, "TRAC".

For this program, the Slab Core Test Facility (SCTF) was also constructed to investigate the two-dimensional thermo-hydrodynamic behavior in the core and the upper plenum. Both facilities are used to achieve the above mentioned task.

The REFLA system code is under development at JAERI and a one-dimensional reflood analysis code, REFLA-1D[6], is currently operational. In order to evaluate the reflood phenomena in reactors, it is important to establish a sufficient data base for realistical modeling of the refill and reflood phenomena which can then be extrapolated to real reactors.

The objectives of this study are to examine the system model required for the best-estimate analysis of the reflood phase of a PWR-LOCA by reviewing the experimental results from the CCTF test C1-5 (Run 14). The selected CCTF test was designated the base case test and used as a reference data base for other parametric effect tests in which some parameters of the experimental conditions were varied. For this purpose, a simplified model was derived by simplifing the well known evaluation model (EM) in a PWR safety analysis. And it is compared with the results of a CCTF test in order to examine the necessity for improvement of the model.

The simplified model is defined as follows:

(1) The core and the downcomer thermo-hydrodynamic behavior are one-dimensional.
(2) No water is allowed to accumulate in the upper plenum.
(3) Each intact loop has the same flow characteristics.
(4) All the water entering the hot legs is evaporated in the steam generators and is heated up to the temperature of the secondary side of the steam generators and is heated up to the temperature of the secondary side of the steam generators.
(5) No parallel channel oscillation occurres in the loops.
(6) The superheated steam is condensed by the subcooled emergency core cooling (ECC) water without dynamic oscillations due to thermo-hydrodynamic coupling.

Main results of the CCTF base case test C1-5 (Run 14) are shown in Appendix B.

II. Preliminary discussion of the system effect in PWR

The core heat transfer during the reflood phase is strongly dependent on the flooding rate, the system pressure and the initial clad surface temperature of the core. Speciafically, the flooding rate is affected by a "steam binding" phenomena, that is, the suppression of the flooding rate by an increase of back pressure of the core due to the vent loss of the steam generated in the core.

The reflood phenomena is a relatively slow transient and is assumed to be in a steady state condition. In a steady state condition, the mass and the momentum balance relations in the system shown in Fig. 1 can be written as follows:

$$\dot{m}_F = \dot{m}_C + \dot{m}_U + \dot{m}_L \ , \tag{1}$$

$$\dot{m}_L = \dot{m}_B + 3 \times \dot{m}_I \ , \tag{2}$$

$$\Delta P_D - \Delta P_C - \Delta P_U = \Delta P_I \ , \tag{3}$$

$$\Delta P_I = (K_I / 2\rho S_L^2)\dot{m}_I \ , \tag{4}$$

$$\Delta P_B = (K_B / 2\rho_B S_L^2)\dot{m}_B \ , \tag{5}$$

$$\Delta P_B - \Delta P_I = \Delta P_{BCN} \ , \tag{6}$$

Using the above equations, the flooding mass flow rate, $\dot{m}_F$, is derived as

$$\dot{m}_F = \dot{m}_C + \dot{m}_U + (\sqrt{(1+\Delta P_{BCN}/\Delta P_I) 2\rho_B / K_B} + 3\sqrt{2\rho_I / K_I}) S_L \times \sqrt{P_D - P_C - P_U} \ . \tag{7}$$

Though, in Eq. (1), $\dot{m}_F$ is expressed with the downstream values of the core, $\dot{m}_F$ can also be expressed with the upstream values of the core as follows:

$$\dot{m}_F = \Sigma \dot{m}_{DL} - \dot{m}_D - \dot{m}_O + \dot{m}_{ECC/LP} \ , \tag{8}$$

where $\dot{m}_{DL}$ is obtained from the following mass and energy balance relations at each ECC port under the assumption of thermal equilibrium:

$$\dot{m}_{DV} + \dot{m}_{DL} = \dot{m}_{ECC} + \dot{m}_{I} \ , \tag{9}$$

$$(\dot{m}_{DV} + \dot{m}_{DL})i = \dot{m}_{ECC}i_{ECC} + \dot{m}_{I}i_{I} \ , \tag{10}$$

$$\left.\begin{array}{ll} \text{if} \quad i_g \geq i \geq i_\ell \ , & (\dot{m}_{DV} + \dot{m}_{LD})i = \dot{m}_{DV}i_g + \dot{m}_{DL}i_\ell \\ \text{if} \quad i > i_g \ , & \dot{m}_{DL} = 0 \ , \\ \text{if} \quad i < i_\ell \ , & \dot{m}_{DV} = 0 \ . \end{array}\right\} \tag{11}$$

(i_ℓ and i_g are enthalpies of liquid and vapor at the saturation temperature, respectively.)

The values of $\dot{m}_C$, $\dot{m}_D$ and $\dot{m}_U$ can be evaluated with the differential pressure ΔP_C, ΔP_D and ΔP_U, respectively, as follows:

$$\dot{m}_n = d(\Delta P_n S_n/g)/dt \quad (n : C, D, U) \ . \tag{12}$$

The values of $\dot{m}_O$ can also be evaluated in a similar manner for the containment vessel, however, the resolution of the ΔP_O measurement is not sufficient to obtain the good accuracy of $\dot{m}_F$ since a large cross section, S_O, of the containment vessel is necessary to catch the large amount of steam and water flowing from the pressure vessel. Therefore, a more precise instrument for measuring the liquid level is necessary. The value of $\dot{m}_O$ can be obtained from the liquid level x, as,

$$\dot{m}_O = d(x\rho_\ell S_O)/dt \ . \tag{13}$$

The fluid temperatures can be measured with thermocouples immersed in the fluid and the enthalpies i_I, i_{ECC} can be estimated. The total mass flow rates in the intact and broken loops, $\dot{m}_I$ and $\dot{m}_B$ respectively, can be measured with Pitot tubes located downstream of the exit of the steam generators, if the entrained liquid is completely evaporated in the steam generators as assumed in the simplified model described in Introduction. The ECC mass flow rates, $\dot{m}_{ECC}$ and $\dot{m}_{ECC/LP}$ are measured

with the flow meters. Since the pressures are measured, i_ℓ and i_g can be estimated from the saturation temperature of the pressure. Therefore, $\dot{m}_F$ can be estimated with either Eq. (1) or Eq. (8).

III. Experiment

1. Apparatus

The functional requirements of this test facility are to provide integral system simulation and systematic measurements of the refill and reflood phenomena. The facility simulates a 1000 MWe PWR with a cold leg break and has a full length pressure vessel which includes a core, a downcomer, and lower and upper plenums. The reference reactors are the Trojan[1] reactor in U.S.A. and, in certain aspect, the Ohi reactor in Japan. The facility also consists of four full-length primary loops with active steam generators and pump simulators. The core consists of thirty-two 8×8 rod bundles which are electrically heated and models a typical 15×15 fuel assembly of a PWR. They are arranged in a cylindrical configuration to minimized the wall effect, i.e., the effect of wall surrounding core on the thermo-hydrodynamics.

Volumetric scaling of the system is based on a core area scaling ratio of 1/21.4. The axial peaking factor is about 1.49. Each bundle consists of fifty-seven heated rods and seven non-heated rods. The heated rods consists of twelve high, seventeen medium and twenty-eight low powered rods with power ratios of 1.1, 1.0 and 0.95, respectively. The core is divided into three power zones (the center has the highest power density and the peripheral has the lowest power density). The cross section of the pressure vessel is shown in Fig. 2. The downcomer gap is 61.5 mm and the flow area of the core baffle is included in the downcomer flow area. The vessel wall is heated up to a preset temperature to simulate the hot wall effects. The design of the upper plenum internals is based on the old Westinghouse design for 17×17 array fuel assemblies. The internals consists of twelve control rod guide tubes, four support columns, eight short stubs, two orifice plates and six open holes. The radial dimensions of each internal is scaled down by a factor of 8/15 from that of an actual reactor.

The steam generators are of the U-tube and shell type. The tube length is about 15 m and about 5 m shorter than that of an actual reactor. The secondary side is filled with high pressure saturated water. The pump simulators are equipped with orifice plates to simulate the flow resistance of a locked pump with fixed vanes to simulate counter-current flow limited (CCFL) characteristics of the locked pump. The location of

the loop seal is a U-tube-shaped piping which connects with the outlet plenum of the steam generator and the suction side of the pump.

The containment vessel is simulated with two tanks, i.e. Containment tanks 1 and 2. The former is used for the water collector vessel and is equipped with a steam/water separator and a liquid level meter to measure the discharge rate, $\dot{m}_0$, as shown in Fig. 1, from the broken cold leg nozzle. Since, a large volume is necessary to represent a scaled containment volume, the pressure of these tanks are maintained to be constant, by means of a pressure control system. Thus, the pressure-time behavior of the PWR containment vessel during a LOCA is not simulated. Containment tank 1 with the steam/water separater is connected to the broken cold leg nozzle and Containment tank 2 is connected to the broken cold leg and to Containment tank 1. The steam in Containment tank 2 is exhausted to the atmosphere through the pressure control valve. In this facility, the break location was assumed to be at the outer surface of the biological shield. A section of cold leg piping about 2.0 m long is connected to the broken cold leg nozzle and the fluid is discharged from the pipe into the Containment tank 1 through a pipe of double size.

The main dimensions of the CCTF and typical PWR are listed in Table 1.

2. Instrumentation

Many differential pressure transducers and thermocouples were installed to measure the differential pressures, fluid temperatures and wall temperatures. In the places where the velocity of liquid phase is very low, the frictional loss and the acceleration loss are negligible compared with the gravitational loss. Hence it is considered that the pressure drops expressed in the water head indicate the collapsed water level or the water accumulation in the downcomer, the core, the upper plenum and the lower plenum. Flow meters were equipped to measure the injection flow rates.

For mass balance calculations, the precision liquid level meter with a servo-tracking mechanism and a direct-coupled digital encoder is capable of giving a resolution of 0.001 cm. The digital signal is fed directly into the digital data acquisition system. The Pitot tubes are positioned at the downstream side of the exit of the steam generators. About 900 thermocouples are uniformly attached on the clad surface of the simulated

core in order to determine whether the thermo-hydrodynamic behavior in the core is one-dimensional or not. Sheathed thermocouples of 0.5 mm diameter are embedded on the outside clad surface. Including other detectors, more than 1600 channel of data were recorded in digital form.

Additionally video cameras, 16 mm movies and 35 mm still cameras are used to observe the flow behavior through view windows located in the primary loops, the downcomer wall and the upper plenum.

3. Test procedure

The test procedures were as follows: After establishing the initial conditions of the test, the lower plenum was filled with saturated water to a specified level of 0.9 m for this test. Electric power was supplied to the heated rods of the core. When the maximum temperature or rods reached the specified temperature, the water in the accumulator was injected into the lower plenum (ACC/LP mode). When the water was estimated to reach the bottom of the core, decay of the heating power was scheduled to be automatically started at a programmed rate, corresponding to the reactor decay heat. After the assumed time delay, the injection location was changed from the lower plenum to the ECC ports of the three intact cold legs. The ECC water was still supplied from the accumulator and this period is defined as the accumulator injection mode (ACC mode). After a specified time delay, the injection mode was transferred from the accumulator injection mode to the low pressure coolant injection mode (LPCI mode). The system pressure of the Containment tank 2 was kept constant. The test conditions of the base case test are listed in Table 2. The power was supplied individually to three radially divided power zones of the core as shown in Fig. 2 and the ratio of the power supplied to a rod of three zones were 1.15, 1.10, and 0.89.

Table 1 Main dimensions of CCTF and a typical PWR

	PWR[1]	CCTF	Ratio
< Length (m) >			
Heated length	3.66	3.66	1/1
Diameter of heated rod	10.7×10^{-3}	10.7×10^{-3}	1/1
Diameter of non-heated rod	13.8×10^{-3}	13.8×10^{-3}	1/1
Rod pitch	14.3×10^{-3}	14.3×10^{-3}	1/1
Distance from the bottom of cold leg nozzle to the bottom of the heated core	4.849	4.849	1/1
Distance from the top of the heated core to the top of the core support plate	0.357	0.357	1/1
Downcomer length	6.066	6.066	1/1
Distance from the bottom of the vessel to the bottom of the heated core	-	2.1	
< Flow area (m^3) >			
Core	5.29	0.260	1/20.3
Downcomer	2.47	0.197	1/21.4
Core baffle	1.76		
Upper plenum	11.10	0.678	1/16.4
Containment tank 1	-	4.906	
Primary loop	0.487∿0.383	0.019	1/25.8∿1/20.3
< Folume (m^3) >			
Lower plenum*	29.6	1.38	1/21.44
Upper plenum	43.6	2.04	1/21.44

* Including the downcomer region below the bottom of core.

Table 2 Test conditions

Items	Values for base case test	Values for PWR
System pressure	0.2 MPa	0.15～0.25 MPa[2]
Initial average linear power	1.4 kW/m	1.34～1.37 kW/m[3]
Radial power factor	1.15	1.435[1]
Axial peaking factor	1.49	1.546[1]
Local power factor	1.1	1.027[1]
Total peaking factor	1.885	2.278[1]
Decay curve of power	ANS×1.2 + Actinide×1.1	ANS×1.2 + Actinide×1.1 + Delayed neutron[1]
Maximum initial clad temp.	873 K	1143 K[1]
Downcomer wall temp.	471 K	443 K[5]
Other wall temp.	392 K	-
Steam generator secondary side water temp.	538 K	538 K[4]
K factor of primary loop	25	24.45[4]
ECC injection conditions		
ACC flow rate	$7.78\times10^{-2}m^3/s$	$(7,97\sim10.5)\times10^{-2}m^3/s$[4]
ACC water temp.	308 K	308 K
ACC injection period	14 s	14 s
LPCI flow rate	$8.33\times10^{-2}m^3/s$	$1.11\times10^{-2}m^3/s$[4]
LPCI water temp.	308 K	308 K

Note

1) Sendai Unit 1.[2]
2) Takahama Unit 3 & 4.[3]
3) Trojan 2 % overpower, 30 seconds after shutdown with power decay function for Takahama & Sendai.
4) Conditions referred in FLECHT-SET tests.[4]
5) Equivalent wall temp. erature, see Appendix.

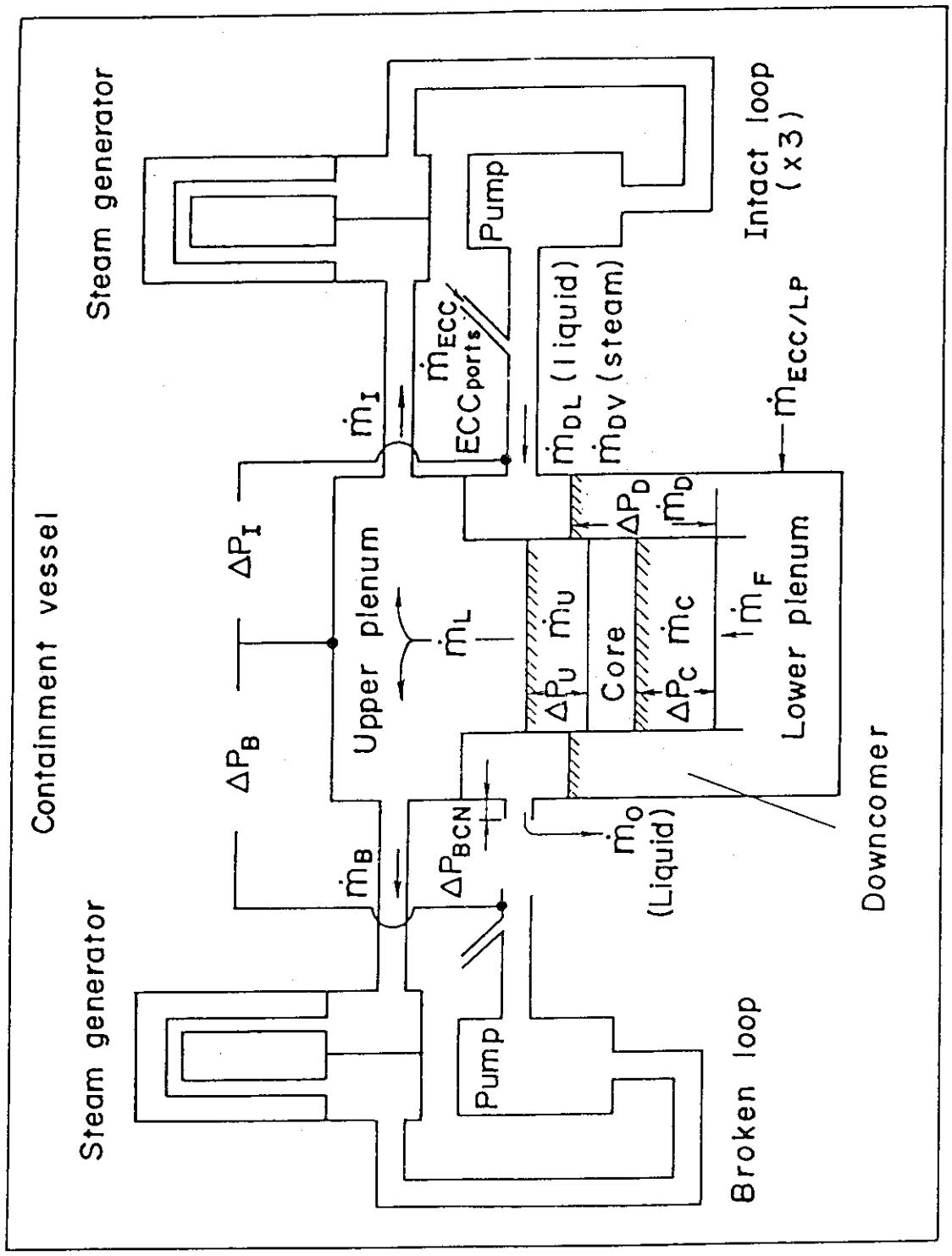

Fig. 1 Mass and momentum balance in PWR system

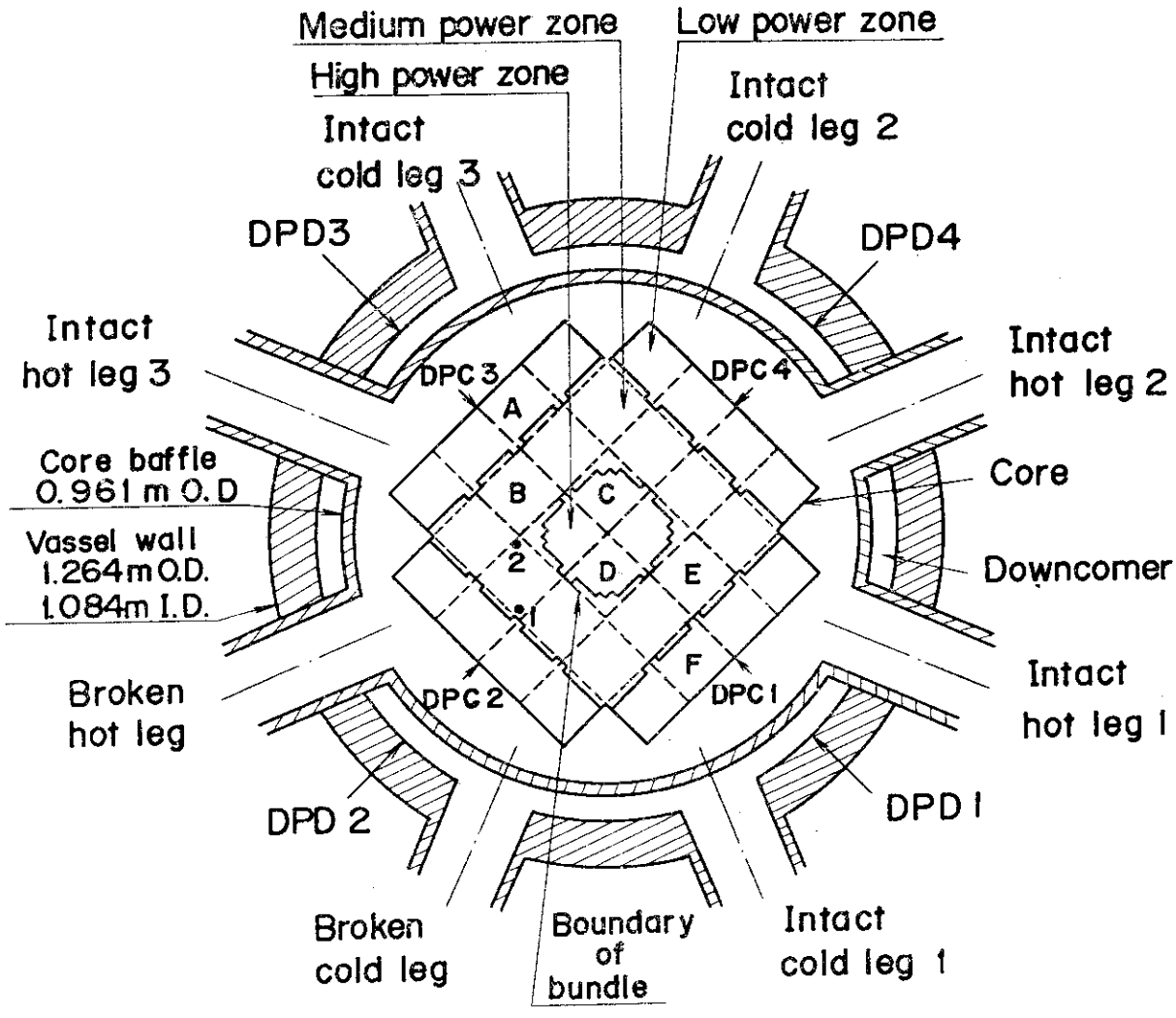

Fig. 2 Cross section of pressure vessel

IV. Results and Discussion

1. Chronology of events and results of the visual observations

The chronology of events is presented in Table 3. The ACC injection period was 13 seconds and the power decay was initiated at 1 second after the reflood initiation.

The flow behavior was monitored with video cameras and 16 mm movies. The observed results were as follows: At 66 seconds, the droplets on the view window just above the upper core support plate began to be swept away. A liquid film falling down on the surface of the upper plenum structures was detected at 81 seconds. The water began to accumulate in the region below the top surface of the upper core support plate. The surface of the accumulated water gradually rose and reached the top surface of the upper core support plate at 106 seconds. It can be inferred that a fraction of the liquid in the core was entrained by the steam flowing in the core to the upper plenum, partly de-entrained in the upper plenum and eventually accumulated in the region below and above the upper core support plate.

A dispersed or annular flow was observed in the hot legs of the intact and broken loops after 67 seconds as droplets began hitting the view window of the inlet plenum of the steam generator. No water was detected at the loop seal portion of the intact and broken loops. Therefore, it is surmised that the water into the hot leg was completely evaporated in the steam generator and the single-phase steam flowed in the loop seal of the all loops. A flow reversal towards the pump simulator was observed during the ACC injection period, upstream of the ECC ports of the intact cold legs. However, any water was not observed at the bottom of the loop seals. It appears that a flooding phenomena occurred at the vertical pipe below the pump simulator. After switching the ECC injection mode from the ACC to the LPCI mode, the mass of water remaining between the loop seal and the ECC port seems to have been swept to the pressure vessel by 216 seconds. This was based on the response of the signals from thermocouples of the pipe wall between the ECC port and the top of the pump simulator. The thermocouples showed superheat of the wall at this time. A bubbly or separated flow was observed during the ACC injection period at just downstream of the intact cold leg ECC ports, while a dispersed flow was observed during the LPCI injection

period. After 77 seconds, a separated or slug flow was observed at the broken cold leg nozzle and it appeared that the water flow rate then increased with time.

2. Core inlet mass flow rate based on mass balance calculations and its accuracy

Mass balance calculations were performed with Eqs. (1) and (8), since it was found that the water entering the steam generator was completely evaporated. In the differentiation, higher frequency components of the data tends to be amplified more. Therefore, in the differentiation of the differential pressure data, the smoothing procedure was used to suppress the high frequency components of the data. Figure 3 shows the flooding mass flow rates, $\dot{m}_F$s, calculated from Eqs. (1) and (8) by averaging data in 20 seconds.

In the ACC injection period, the calculated values, $\dot{m}_F$s, are significantly different from each other. This discrepancy may be caused by in accuracy of the mass flow rate injected into the system and by the unaccounting of the storage of water in the cold leg pipe. The former might be introduced from the slow time response (time constant 1 second) and the change of the gas volume in the injection line. In this period, specially before the steam generation from the core became noticable, the mass flow rate, $\dot{m}_F$, calculated with Eq. (1) is reasonable, since the calculation needs the increasing rates of the masses in the core and the upper plenum and their accuracy is enough for our estimation.

In the LPCI injection period, the calculated values, $\dot{m}_F$s, are slightly different from each other. Judging from the time-integral values of both $\dot{m}_F$s, their average values are nearly proportional. The discrepancy was inferred to be caused by the disregard of the bypass of steam and liquid from the upperplenum without going through the hot legs in the calculation with Eq. (1). And additionally the discrepancy was caused by the disregard of the steam generation in the downcomer due to the hot wall of the pressure vessel in the calculation with Eq. (8). It was estimated that the disregard of the downcomer steam generation was caused the error of 0.25 kg/s on predicted $\dot{m}_F$. The estimation was made by comparing the results of the tests with hot and cold downcomer conditions. In the LPCI injection period except for the early period, the mass flow rate, $\dot{m}_F$, calculated with Eq. (8) is reasonable, since the error from the injected

ECC flow rate measurement is negligible under the quasi-steady state condition appeared in this period and the error caused by the steam generation in the downcomer is small.

In order to obtain the best estimate core inlet mass flow rate, the calculation with Eq. (1) were performed by using the corrected values of the loop mass flow rates, $\dot{m}_F$s and $\dot{m}_B$. The correction was made by multiplying $\dot{m}_F$s and $\dot{m}_B$ by a factor which yields identical $\dot{m}_F$s in the calculations with Eq. (1) and (8). Figure 4 shows the best estimate core inlet mass flow rate. In this calculation, the smoothing procedure was performed by averaging $\dot{m}_F$ in 10 seconds. Therefore the core inlet velocity at the reflood initiation was slightly lowered. Since the bypass of steam and water from the upper plenum is difficult to be evaluated quantitatively, this estimation involves at greatest about 15 % error. The relation between the integral core-flooded water mass evaluated with Eqs. (1) and (8) and best-estimated are shown in Fig. C-36 in Appendix C.

3. Core thermo-hydrodynamic behavior

Figure 5 shows four differential pressure transients in the core measured azimuthally every 90 degrees as shown in Fig. 2. No spacial hydrodynamic oscillations were detected. The hydrodynamic behavior seems to be one-dimensional or at least axisymmetric. Figure 6 shows the temperature transient bands measured with every thermocouple attached at the midplane of the average power rods in the each power zone. It is found that the temperature transients in the three power zones are different from each other, however, the quench times at the midplane are approximately the same. The temperature transients of two heated rods are shown in Fig. 7. These rods are located in the medium power zone as shown in Fig. 2. One rod, indentified as 1, is close to the low power zone and the other rod, identified as 2, is close to high power zone. Except for the top thermocouples, the heat transfer characteristics are similar to each other. At the present time, the mechanism for the top quenching is obscure. The top quenching has little influence on the temperature responses of the lower thermocouples and hence, its effect is neglected in this study. Figure 8 shows the propagation of the bottom quench front in the core. The quench fronts are interpolated from the relationship between the measured quench times and the elevations of the five thermocouples attached on the cladding of the rods in the bundles shown in Fig. 2. In the figure,

the bottom quench fronts of the three power density rods in each three power zones are indicated. The quench front is almost radially flat and its propagation can be considered to be roughly one-dimensional and does not significantly depend on the radial power profile.

From the above discussion, it is concluded that for the core thermo-hydrodynamic behavior, in special, the quench front propagation is nearly one-dimensional, while the temperature transient on the cladding is dependent on the heating power.

4. Downcomer thermo-hydrodynamic behavior

In the downcomer, two-dimensional motion of the tiny bubbles in the water was observed through the view window. However, as shown in Fig. 9, the transients of the four differential pressures measured azimuthally every 90 degree overlayed each other. Therefore, it is thought that the water accumulation and the voiding can be treated to be one-dimensional. The water accumulation transient in the downcomer can be divided into the four periods shown in the figure. Period I is the ACC injection period. The time of step A in Period I corresponds to the time of the flow reversal in the cold leg piping due to the switching of the ECC injection ports from the lower plenum to the cold legs. At this time, the water seems to have been accumulated in the cold leg piping. Period II is the complete accumulation period and practically no ECC bypass occurs. The water accumulated in the cold leg piping during time A is almost ejected into the downcomer just after the initiation of the LPCI mode. Period III is the partial ECC bypass period. Judging from the response of the differential pressure transducers in the downcomer, it was recognized that the water level did not reach the spill-over level. However, the overflowed water was detected in Containment tank 1 and the water was recognized to bypass the downcomer. Since some portion of the ECC water entered in the downcomer was considered to be bypassed, this period was defined as the partial ECC bypass period. The bypass mass flow rate is gradually increasing with time up to about 5 kg/s. The bypass mass flow rate seems to depend on the difference between the spill-over level (i.e. the elevation of the bottom of the broken cold leg nozzle) and the liquid level in the downcomer. During Period IV, the water accumulation is roughly terminated and the mass flow rate into the downcomer minus the core inlet mass flow rate is almost the same as the bypass mass

flow rate.

In Period IV, the effective downcomer head is lower than the estimated from the spill-over level. This may be explained with the idea that the bypass mass flow rate increases when the liquid level approaches the spill-over level and the water accumulation terminates when the mass balance among the incoming and outgoing liquid masses is established. But partially, this must be caused by the voiding of the water due to heat released from the hot downcomer wall. The reduction of the effective downcomer head reduces the core flooding rate as described by Eq. (7).

The ECC bypass reduced the water accumulation rate in the downcomer and caused the driving head for the core flooding to become lower as expressed with Eq. (7). In this experiment, the ECC flow rate was about 3/4 of that estimated in the safety analysis[4] and the ECC water is thought to have been not completely accumulated in the downcomer during the ACC injection period. The water seems to accumulate completely during the ACC injection period and ECC bypass is considered not to occur under the higher ECC flow rate situation. Under this situation, a larger amount of subcooled water can be supplied into the downcomer and a higher effective head can be expected. For verification of this assumption, a test with a higher ECC flow rate is necessary.

5. Upper plenum

The water accumulation in the upper plenum is shown in Fig. 10. The shaded area indicates the range of the data measured by the pressure transducers positioned azimuthally every 90 degrees.

The water effluent from the core was accumulating in the space between the top of the heated core and the top of the upper core support plate and then began accumulating in the upper plenum region. About 5 to 15 % of the effluent mass was accumulated in the upper plenum. The water accumulation rate in the upper plenum was 0.48 kg/s at 350 seconds. This indicates that about 10 % of the mass effluent from the core was accumulated in the upper plenum. The water accumulation in the upper plenum results in a higher flooding rate than that predicted by the simplified model as shown in Eq. (7).

The de-entrainment ratio which defines the ratio of the water accumulation in the upper plenum to the water mass flow rate from the core is also indicated in the figure. For the derivation of the de-entrainment

ratio, the steam mass flow rate from the core was roughly estimated with the supplied power and the heat release of the stored energy in the core, therefore, the entrainment ratio is a rough estimation. After the overall core is quenched, the heat release of the stored energy in the core becomes negligible and the released heat can be considered to come only from the supplied power. The liquid fraction calculated with Wilson's correlation[7] is indicated in the figure. It was assumed in this calculation that the water level was equal to the elevation of the bottom of the hot leg nozzle and the mixture was homogeneous. From the figure, at least, after 60 seconds the liquid level seems to reach the elevation of the hot let nozzle. If the stored energy release is considered in the calculation of the steam generation the lower liquid fraction can be expected due to higher steam generation. Accordingly the liquid level is thought to have reached the elevation of the hot leg nozzle in the quenching period.

The liquid level observed through the view window at the periopheral region was higher than the measured water head in the upper plenum while the bubbles in the water below the liquid surface was found to be moving downwards. It appears that more steam ascends and entrains water in the center region. Therefore, it is considered that a fraction of the entrained water was de-entrained and accumulated in the peripheral region. The accumulated water then returned to the center region and was re-entrained with the ascending steam. Thus, the flow behavior seems to be three-dimensional. However, since the behavior can be considered to be a quasisteady state, the hydrodynamic behavior in the upper plenum seems to be able to be treated macroscopically.

6. Loop and broken cold leg nozzle

Figure 11 shows the pressure drop across each loop. Before 6.30 seconds, the pressure drop across the each intact loop, ΔP_I, and that across the broken loop, ΔP_B, are equal to zero. They then begin to increase due to the back pressure caused by the increased steam generation in the core. Since the curves of ΔP_I nearly overlap with each other, the mass flow rates through the intact loops, $\dot{m}_I$s, are nearly indential. Since no parallel channel oscillation was observed, it is not necessary to consider the dynamic coupling phenomena among the three

intact loops. The curve of ΔP_B deviated from the curves of ΔP_I at 77 seconds and at the same time the water flow was observed in the broken cold leg nozzle. $(\Delta P_B - \Delta P_I)$ corresponds to the pressure drop at the broken cold leg, ΔP_{BCN}. As the water and the steam flow rate increased at the nozzle, ΔP_{BCN} and the pressure drop at the nozzle itself increased and had the same tendency as the acceleration loss at the broken cold leg nozzle as estimated on the basis of the homogeneous fluid model as shown in Fig. 11. The discrepancy between the measured and estimated values may be caused by the friction loss along the broken cold leg piping connected to the nozzle. The higher ΔP_{BCN} makes the flooding rate, $\dot{m}_F$, higher as indicated in Eq. (7). Figure 12 shows the fluid temperature responses in the steam generator of the intact loop 1. The bulk fluid temperature in the secondary side of the steam generator is 538 K while the fluid temperature in the inlet plenum is 393 K which is the saturation temperature. The pressure drop across the steam generator in the primary system was so small that the saturation temperature in the outlet plenum was almost the same as that in the inlet plenum. The fluid temperature in the outlet plenum was about 500 K after 120 seconds. The predicted value of the fluid temperature in the outlet plenum, assuming a heat transfer coefficient of single phase gas flow, is about the same as the measured value.

In the present simplified model, the exit steam is assumed to be superheated to the fluid temperature in the secondary side of the steam generator. The measured fluid temperature in the outlet plenum is about 40 K lower than that in the secondary side. This results in higher steam densities, ρ_I, and ρ_B, giving a higher flooding rate, $\dot{m}_F$, as derived from Eq. (7). However, the fluid temperature of the secondary side near the outlet plenum was about 410 K and lower than the fluid temperature at the exit of the steam generator. Therefore, in this study it can be only concluded that the fluid temperature at the exit was nearly the same as the fluid temperature of the secondary side.

Figure 13 shows the ECC water injection rate at the intact cold leg 1, the steam mass flow rate from the steam generator to the ECC port and the temperature of the ECC water. The reduction of the ECC water injection rate at 76 seconds is due to the switch from the ACC mode to the LPCI mode. The spike in the fluid temperature at 73 seconds is due to the discharge of the saturated water stored in the ECC line. No significant

oscillatory behavior could be observed in the fluid temperature at the ECC port and the differential pressure across the intact cold legs as shown in Fig. 13 and Fig. 11, respectively. The fluid temperature measured at downstream of the ECC port is almost the same as the calculated value based on the thermal equilibrium model with the assumption of complete mixing of the injected water with the steam from the steam generator as shown in the figure.

7. Summary

The phenomena observed in the referred test were similar to the simplified model which is similar to but slightly simplified evaluation model (EM) as described in Introduction, i.e.,

1. The temperature transients of the same powered rods in the core are about the same. The quench front is almost radially flat and propagates roughly one-dimensional. No spacial hydrodynamic oscillations exist in the core.
2. The downcomer water accumulation behavior is nearly one-dimensional.
3. Each intact loop has similar flow characteristics and no parallel channel oscillation was observed.
4. All the water entering the hot legs was evaporated in the steam generator and was heated to nearly the same temperature as the fluid temperature in the secondary side during the concerned period.
5. The superheated steam is condensed by the subcooled emergency core cooling water without dynamic oscillations due to the thermo-hydrodynamic coupling.

The following points were different from the simplified model:

1. In the upper plenum about 5 to 15 % of the total effluent from the core was accumulated. This corresponds to water accumulation of 8 to 30 % of the liquid flowing from the core. The value was estimated from a rough calculation.

The liquid level of the peripheral region seems to have reached the bottom of the hot leg in the later period of the experiment. The collapsed water level of this period seems to be able to be expressed with the void fraction correlation similar to Wilson's correlation[7]. The water accumulation in the upper plenum makes the core flooding rate higher as

expressed by Eq. (7).

2. ECC bypass was observed in the downcomer after switching from the ACC to LPCI injection before the water accumulation terminated. The ECC bypass reduced the water accumulation rate in the downcomer. The bypass mass flow rate seems to depend on the difference between the liquid level and the spill-over level. The slow water accumulation in the downcomer makes the core flooding rate low as expressed by Eq. (7). In this test, the ECC flow rate was too conservative, resulting in incomplete water filling inthe downcomer during the ACC injection period. If the ECC flow rate had been higher, the downcomer might be nearly completely filled in the ECC injection period and the ECC bypass might not appear. In order to examine the above assumption, a test with a higher ECC flow rate is necessary.

The effective downcomer head which means the saturated value was lower than that estimated from the spill-over level, that is, the bottom of the cold leg. The reduction of the effective downcomer head reduces the core flooding rate as expressed with Eq. (7). At the higher ACC flow rate, a larger amount of colder water can be supplied to the downcomer, therefore, a higher effective head can be expected.

3. A significantly large pressure drop was observed at the broken cold leg nozzle and in the interconnected pipes. The pressure drop was thought to be induced by the acceleration and friction losses of water in the broken cold leg. The pressure drop increases the core flooding rate as expressed by Eq. (7).

The pressure drop is induced in a relatively long pipe (about 2.0 m). The length was determined from the assumption that the break location is just outside of the biological shield. However, it should be not that about half of the pressure drop is produced near the broken cold leg nozzle (within 0.4 m from the nozzle).

The difference between the simplified model and EM is little for the system model, i.e. the finite heat transfer was assumed for the steam generators in EM, while the equal fluid temperature to the secondary fluid temperature is used at the primary outlet plenum of the steam generator in the simplified model.

Therefore, it can be concluded that observed phenomena are similar to the EM with exception mentioned above.

Table 3 Chronology of events

Items	Time after experiment initiated (s)
Power supply initiated	0
ACC/LP mode initiated	52.5
Initiation of reflood phase	63
Decay of power initiated	64.5
Swiched from ACC/LP mode to ACC mode (cold leg injection)	67
LPCI mode initiated	76
Turnaround temperature (1045 K) observed	141
All heated rods quenched	594.5

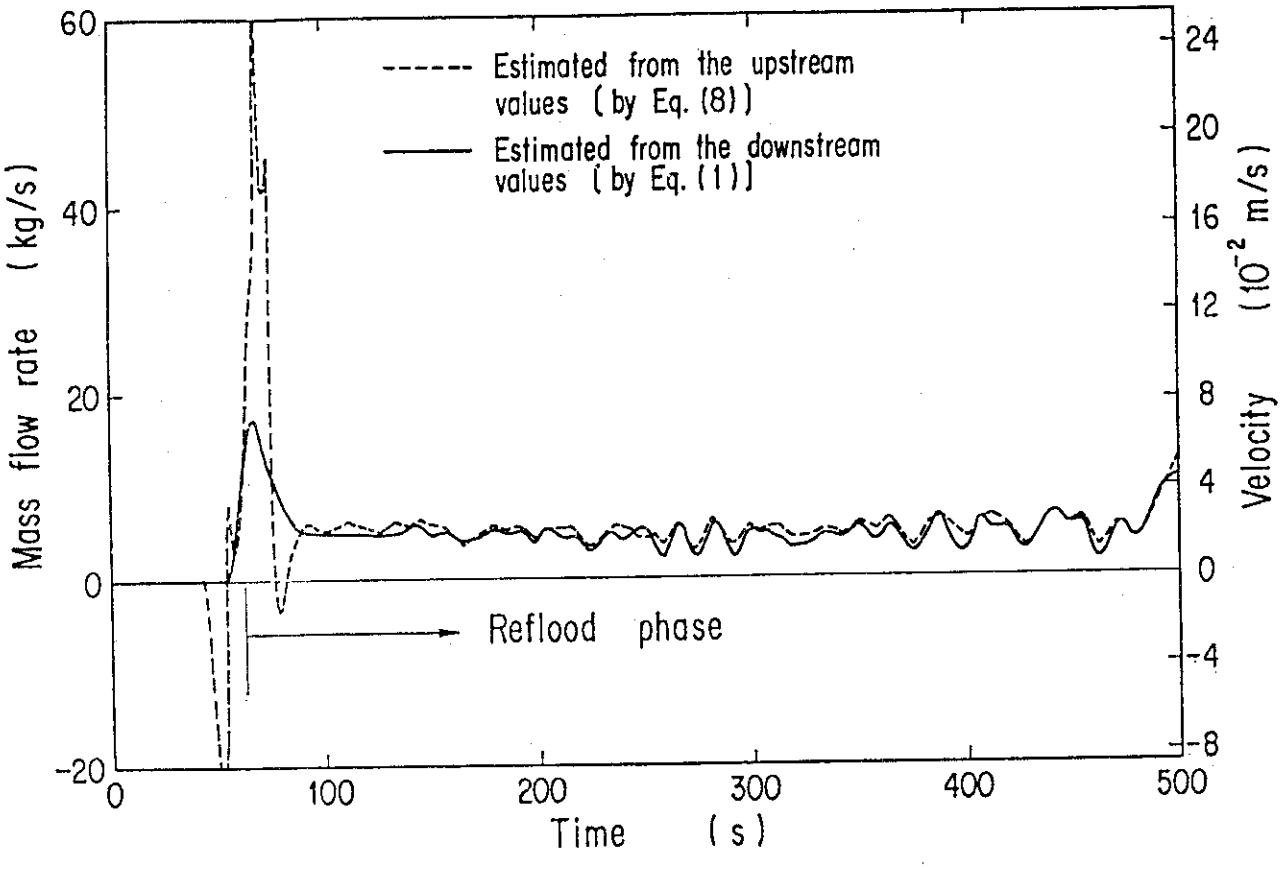

Fig. 3 Core flooding mass flow rates evaluated with Eqs. (1) and (8)

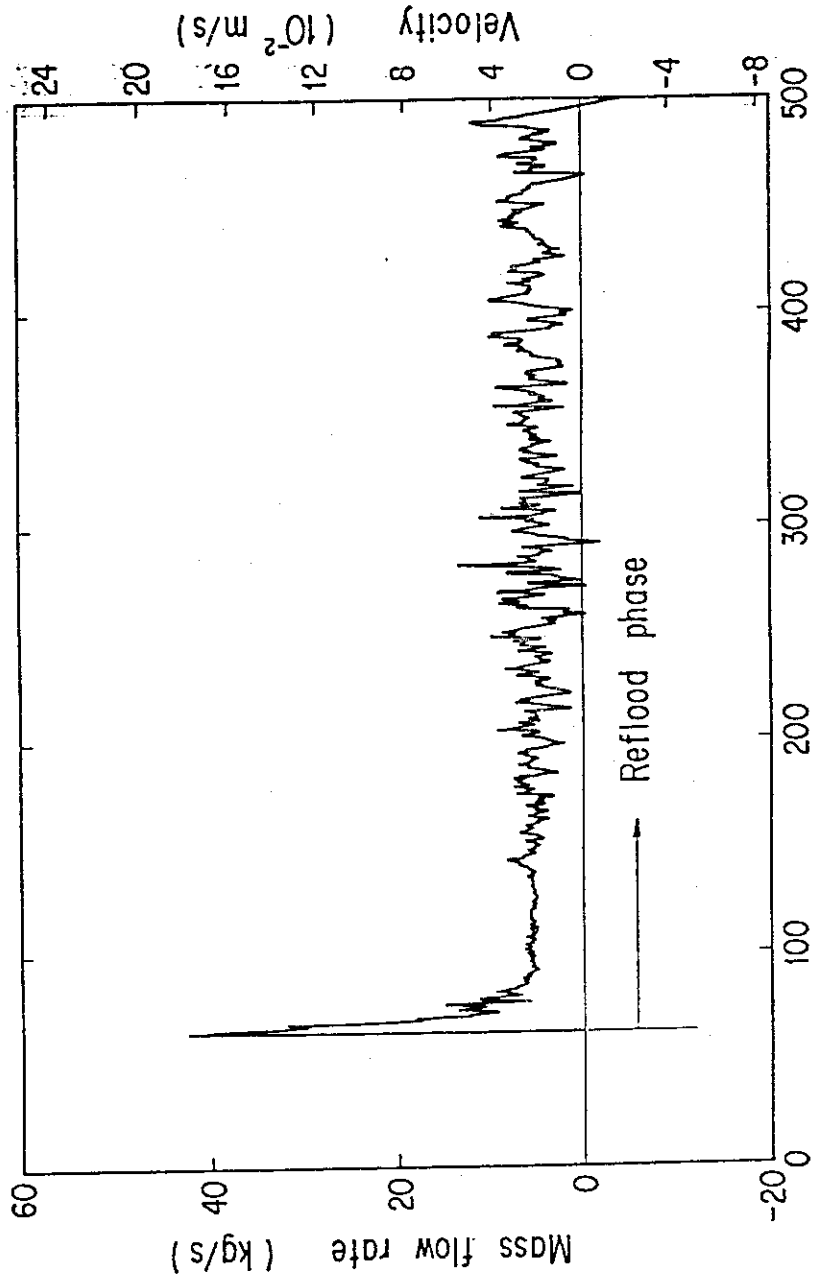

Fig.4 Best estimate core flooding mass flow rate

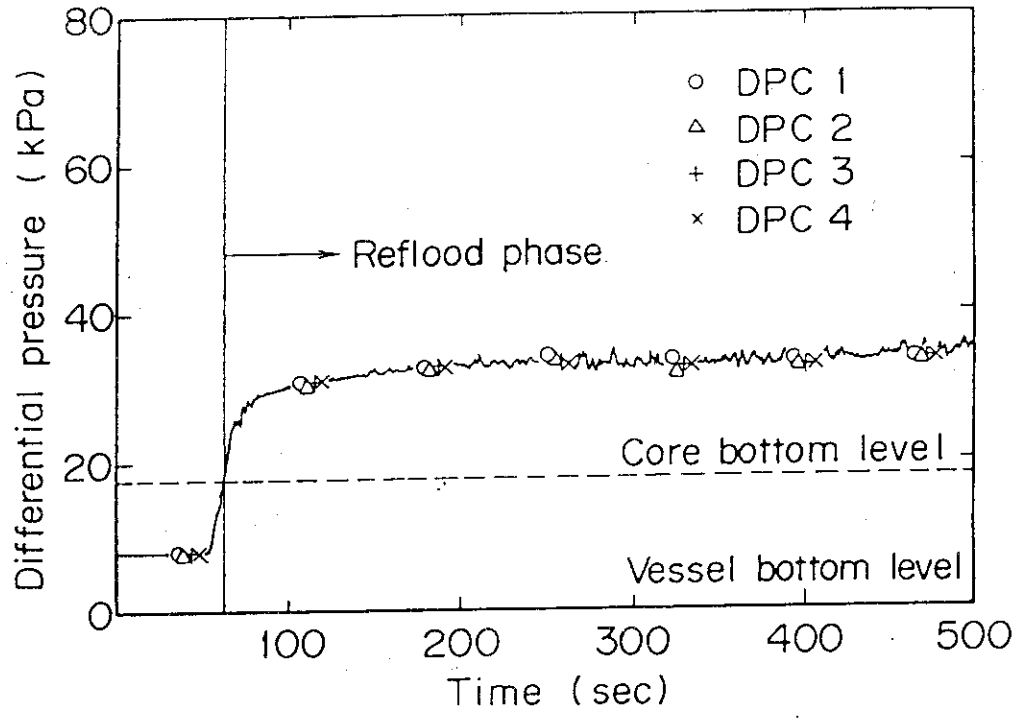

Fig. 5 Symmetry of differential pressure transients in core

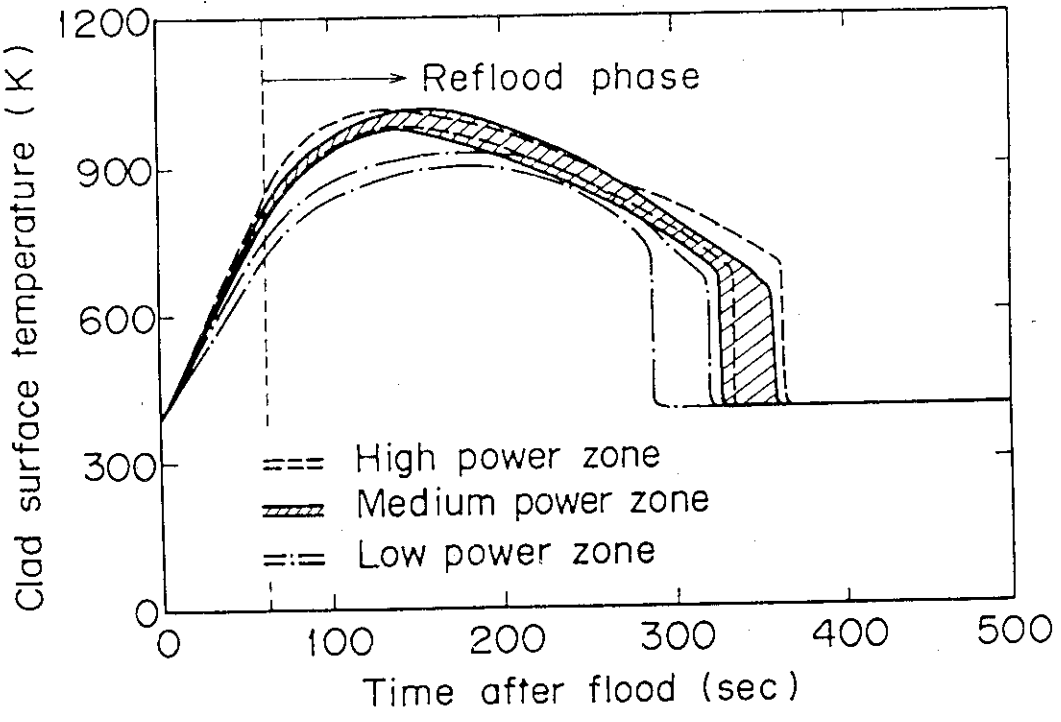

Fig. 6 Temperature transients on clad surface of medium power rods in three power zones

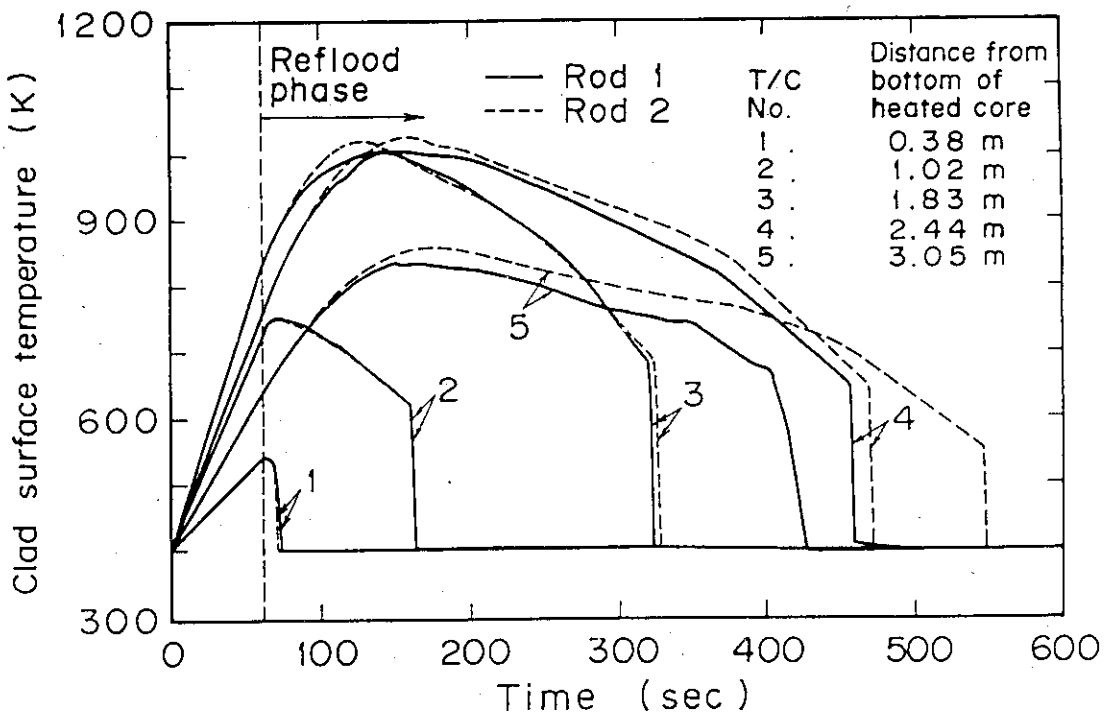

Fig. 7 Similarity of temperature transients in same power zone

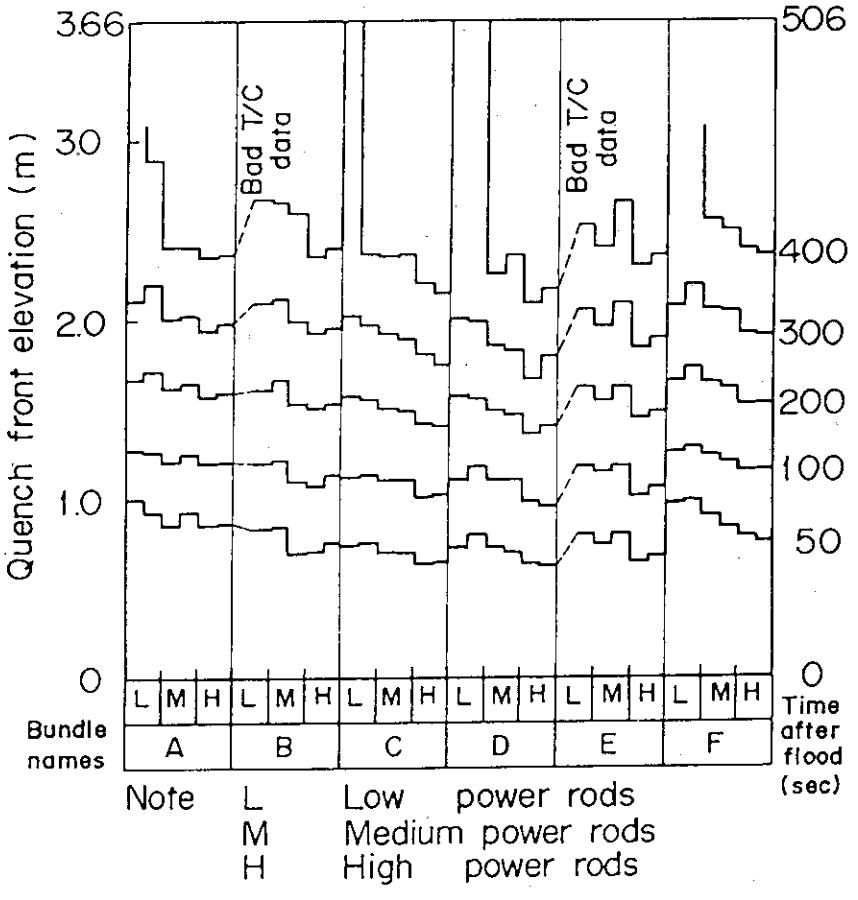

Fig. 8 Propagation of bottom quench fronts

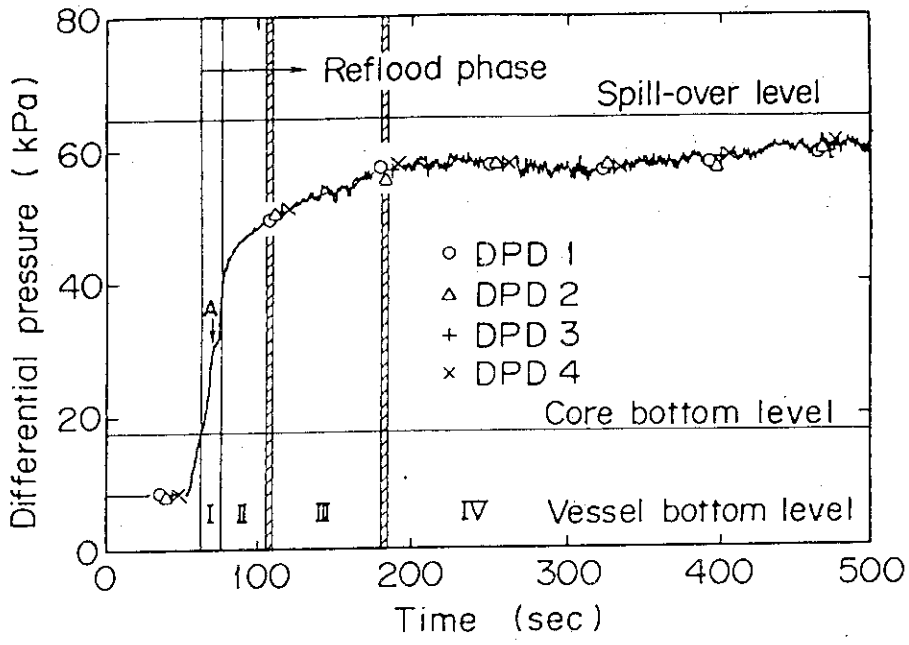

Fig. 9 Symmetry of differential pressure transients in downcomer

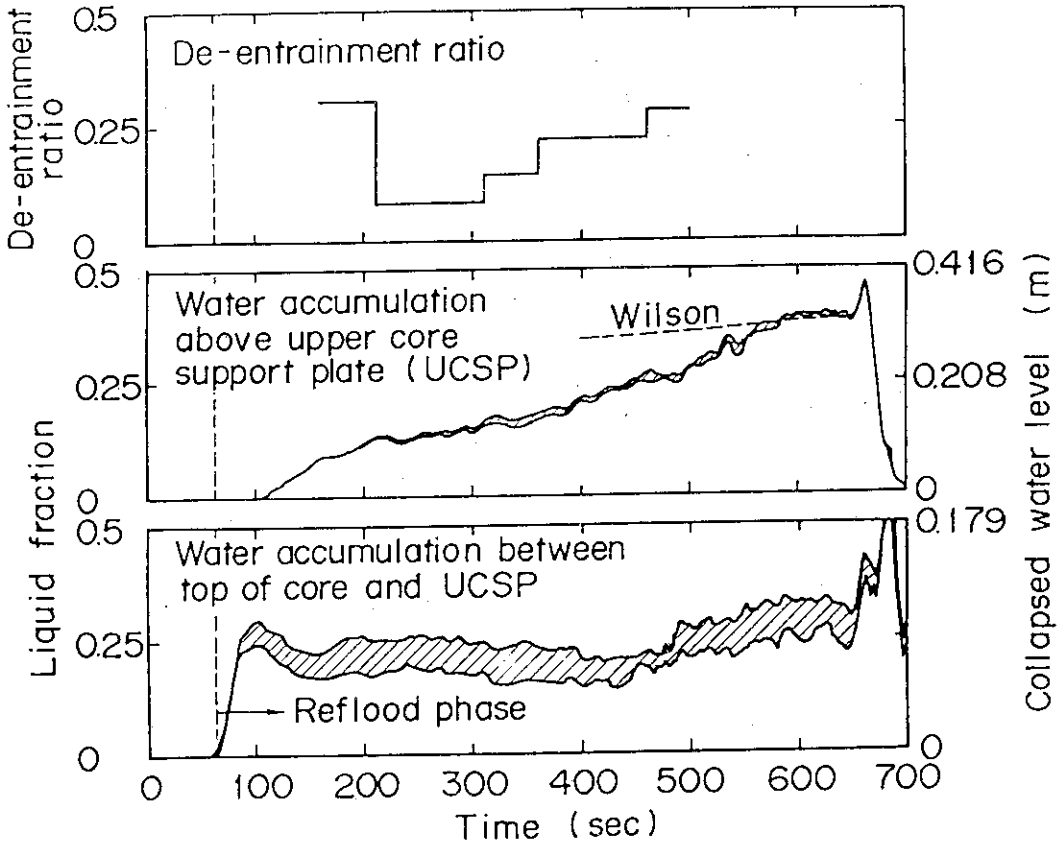

Fig. 10 Water accumulation behaviors in upper plenum

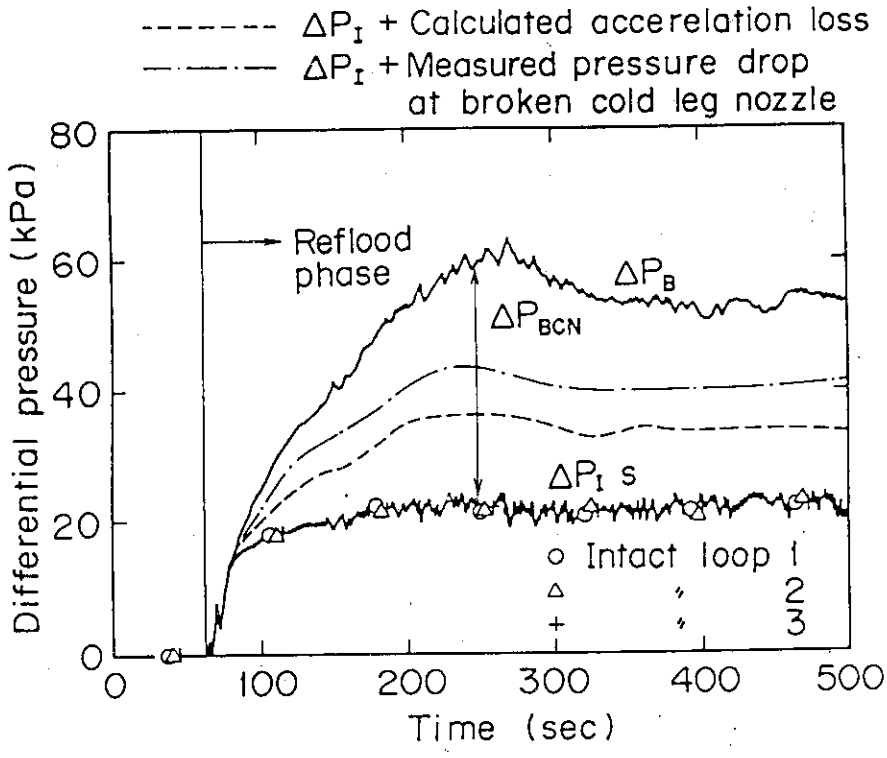

Fig. 11 Pressure drops across loops

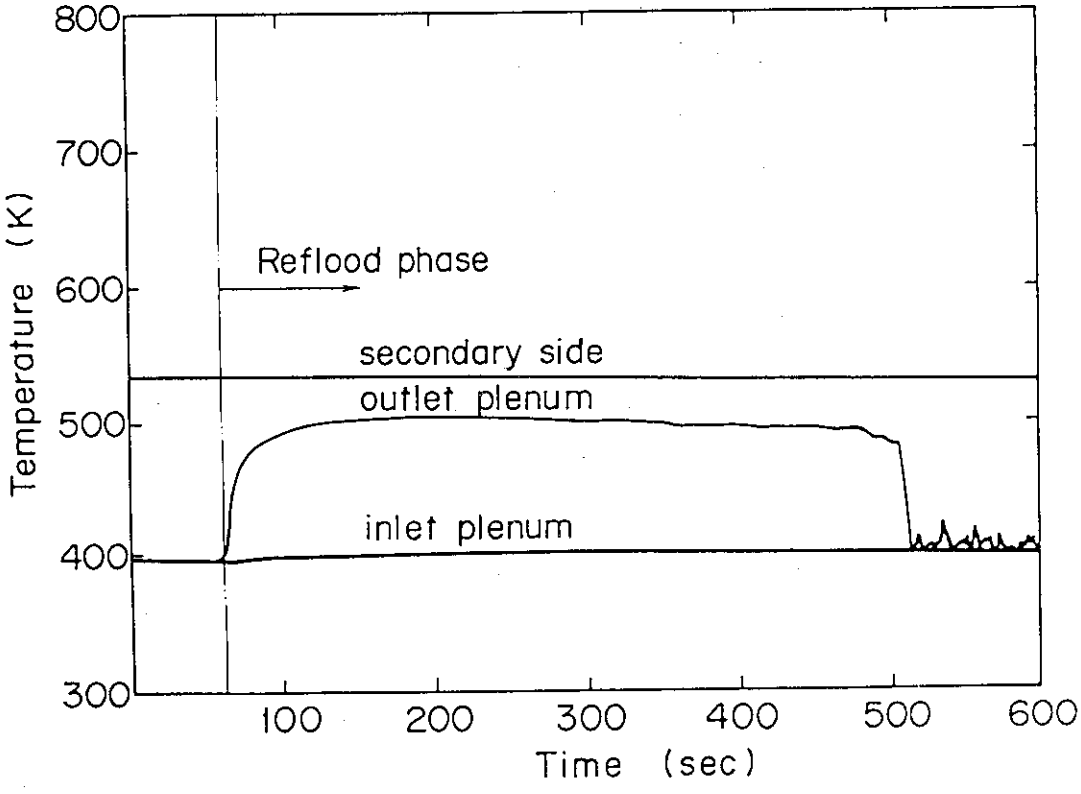

Fig. 12 Fluid temperatures in a steam generator

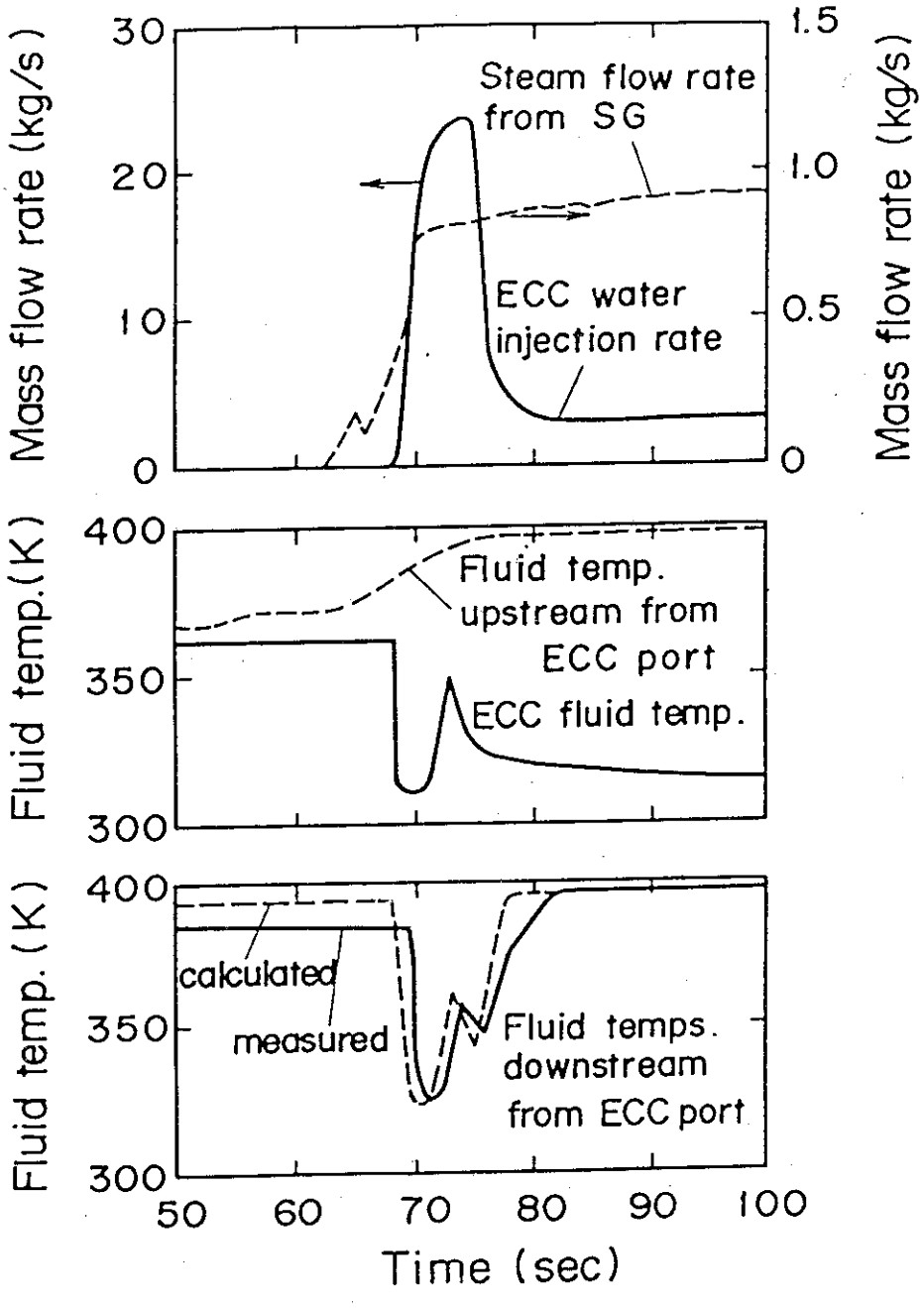

Fig. 13 Flow behavior around an ECC port

V. Conclusion

1. The phenomena observed in the referred test were similar to the simplified model for the best-estimate system model as described in Introduction.

2. The different points were (1) the water accumulation in the upper plenum, (2) the ECC bypass in the downcomer, (3) the reduction of effective downcomer head and (4) the pressure drop at the broken cold leg nozzle and in the interconnected pipe. They are also described in summary.

3. Since the difference between the simplified model and the evaluation model (EM) for the system model are small, the different points described in conclusion 2 also apply to the EM.

4. Since it is considered that the points (1) and (4) in Conclusion 2 gave higher flooding rates than that in the safety evaluation, the points (2) and (3) in Conclusion 2, however, gave the opposite effects. Since the points (2) and (3) are considered to have been resulted from a too conservative ECC flow rate, another test with a higher ECC flow rate is necessary to investigate these problems.

[Nomenclature]

i	:	Enthalpy (J/kg)
i_g	:	Enthalpy of saturated steam (J/kg)
i_ℓ	:	Enthalpy of saturated water (J/kg)
K	:	Factor of flow resistance of a primary loop ($\equiv \Delta P / \frac{1}{2} \rho v^2$)
m	:	Mass flow rate or mass accumulation rate (kg/s)
S	:	Flow area or cross section (m^2)
S_L	:	Flow area of each primary loop piping (m^2)
S_O	:	Cross sectional area of carry-over measuring tank (m^2)
t	:	Time (s)
V	:	Velocity (m/s)
ΔP	:	Pressure drop (Pa)
ρ	:	Density (kg/m^3)

Subscripts

B	Broken loop
BCN	Broken cold leg nozzle and connected pipe
C	Core
D	Downcomer
DL	Liquid through a cold leg into downcomer
DV	Steam through a cold leg into downcomer
ECC	ECC water injected into cold legs
ECC/LP	ECC water injected into a lower plenum
F	Flooded into a core
I	Intact loop
L	Primary loops
O	Carried-over through the broken cold leg nozzle
U	Upper plenum

Acknowledgement

The authors are much indebted to Messrs. T. Iguchi and J. Sugimoto for their technical supports. They would like to express their thanks to Dr. M. Nozawa, Director of Reactor Safety Research Center, and Drs. S. Katsuragi and M. Ishikawa, Head and Deputy Head of Division of Reactor Safety Research, respectively, and Dr. K. Hirano, Chief of Reactor Safety Lab.II, for their guidance and encouragement for this program. They also would like to express their appreciation to the 2D/3D project members of USA and FRG, especially Dr. L.S. Tong of USNRC and Prof. Dr. F. Mayinger of T.U. München for valuable discussions.

References

1) Trojan nuclear plant, Final safety analysis report volume 1 ∿ 9, DOCKET-50344-38 ∿ 46, (1973).
2) An audit analysis for evaluation of ECCS of Sendai Nuclear Power Station Unit 1 (in Japanese), Prepared by JAERI, (1977).
3) An audit analysis for evaluation of ECCS of Takahama Nuclear Power Station Unit 3 & 4 (in Japanese), Prepared by JAERI (1978).
4) Waring, J.P. and Hochreiter L.E.: PWR FLECHT-SET Phase B1 evaluation report, WCAP-8583, (1975).
5) Sudo, Y. and Murao, Y.: Experiment of the downcomer effective water head during a reflood phase of PWR LOCA (in Japanese), JAERI-M 7978, (1978).
6) Murao, Y., et al.: REFLA-1D/MODE 1: A computer program for reflood thermo-hydrodynamic analysis during PWR-LOCA User's manual, JAERI-M 9286, (1981).
7) Wilson, J.F. et al.: The velocity of rising steam in a bubbling two-phase mixture, Trans. ANS, vol.5, pp. 151 ∿ 152, (1962).

Appendix A

Estimation of heat released from the hot downcomer wall

The heat released from the downcomer structure of a PWR and for CCTF were calculated with DONTAQ2[5] developed by Sudo. In the calculation, the following assumptions were used:

1) The vessel wall and the core barrel of a PWR are homogeneously heated up to the operating temperature (561 K). The surfaces facing the downcomer starts for follow the saturation temperature of the system pressure calculated in a blowdown analysis, if the temperature becomes lower than the operating temperature. After 22 to 40 seconds, an adiabatic condition was assumed to express the refill period. In this period, the surface temperatures were expected to recover. After 40 seconds, the surface temperature is kept at 393 K (the saturation temperature of 0.2 MPa).
2) The vessel wall of CCTF is homogeneously heated up to the specified temperature. The core barrel of CCTF is kept at 398 K. After reflood is initiated, the wall temperatures are kept at 398 K.

Considering the flow area and the heat transfer area, the equivalent heat flux of a PWR and the heat fluxes of CCTF with various initial wall temperatures of the vessel are shown in Fig.A. From the figure, the best fit initial temperature for simulation of a PWR was considered to be 443 K.

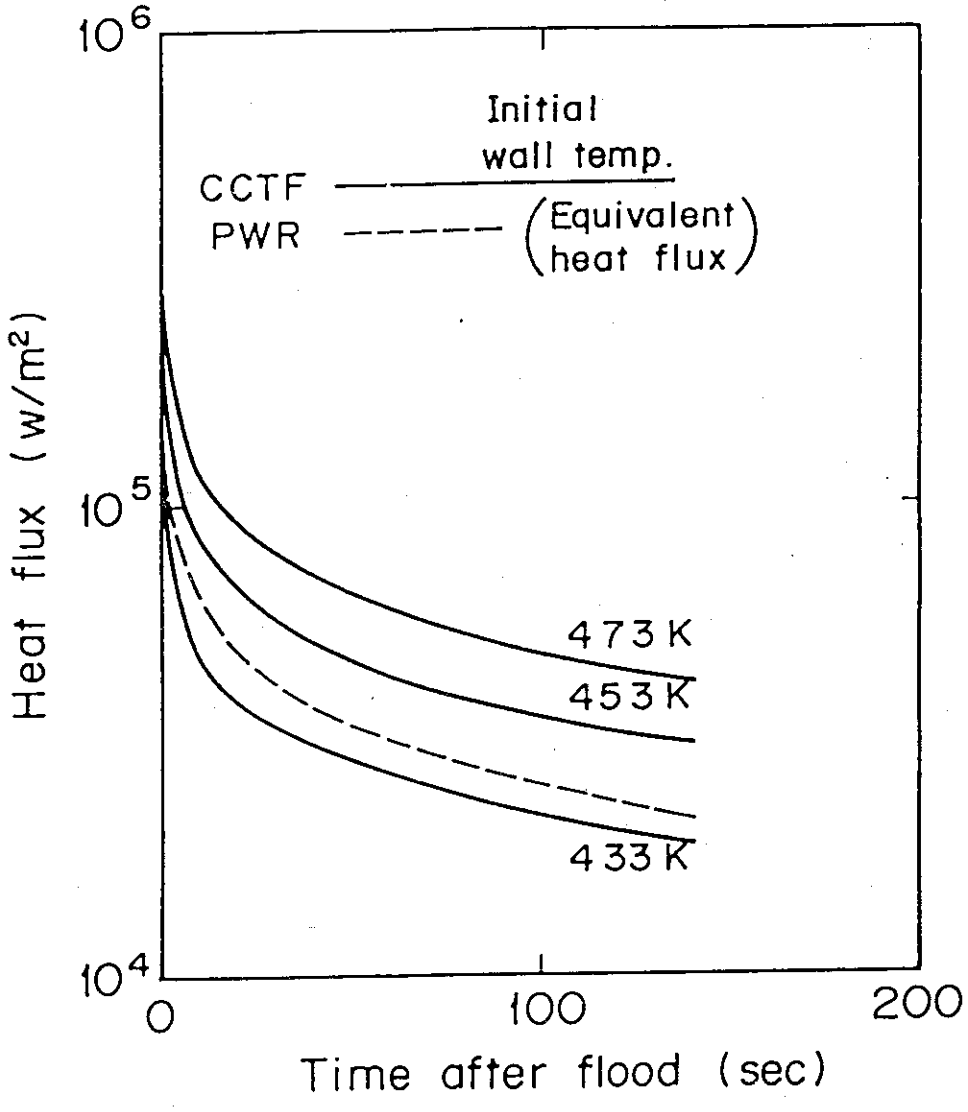

Fig. A Heat flux from the vessel wall of CCTF and equivalent heat flux of a PWR

Appendix B

Explanation of the measuring location of referred data and definition of the evaluated data

Figure list

1. Definition of Tag.ID for clad surface temperatures

Notation : TENNWAM

NN : Bundle number

WA : Power zone

WA = X1, X2 : High power (Local power factor 1.1)

WA = Y1, Y2 : Medium power (Local power factor 1.0)

WA = Z1, Z2 : Low power (Local power factor 0.95)

M : Elevation

	Elevation (m)	Axial power factor
1	0.38	0.568
2	1.015	1.176
3	1.83	1.492
4	2.44	1.312
5	3.05	0.815

2. Definition of power zone and bundle number

See Fig. A-1

3. Definition of Tag.ID for void fraction

See Fig. A-2

4. Definition of Tag.ID for average linear power of heater rod in each power unit zone

See Fig. A-3

5. Definition of carry-over rate fraction (C.R.F)

$$CRF = \frac{\dot{m}_{UP} + \dot{m}_{L}}{\dot{m}_{CR} + \dot{m}_{UP} + \dot{m}_{L}}$$

The calculated data within ±25 s are averaged:

$$(CRF)_i = \frac{1}{101} \sum_{k=i-50}^{i+50} (CRF)_k$$

where

ΔP_{UP} : Average of measured data at four orientations

ΔP_{CR} : Same as above

$$\dot{m}_{UP} = A_{up} \frac{d}{dt} (\Delta P_{UP})$$

$$\dot{m}_{CR} = A_{CR} \frac{d}{dt} (\Delta P_{CR})$$

$$\dot{m}_L = \sum_{k=1}^{4} \dot{m}_{pk}$$

$\dot{m}$: mass flow rate or mass accumulation rate

ΔP: differential pressure

suffix

UP: upper plenum

CR: core

L : loop

p : primary pump

6. Definition of Tag.ID for differential pressure through downcomer, upper plenum, core and lower plenum

   See Fig. A-4

7. Definition of Tag.ID for differential pressure through intact and broken loop and broken cold leg nozzle

   See Fig. A-5

8. Definition of Tag.ID for fluid temperature in inlet and outlet plenum and secondary of steam generator

   See Fig. A-6

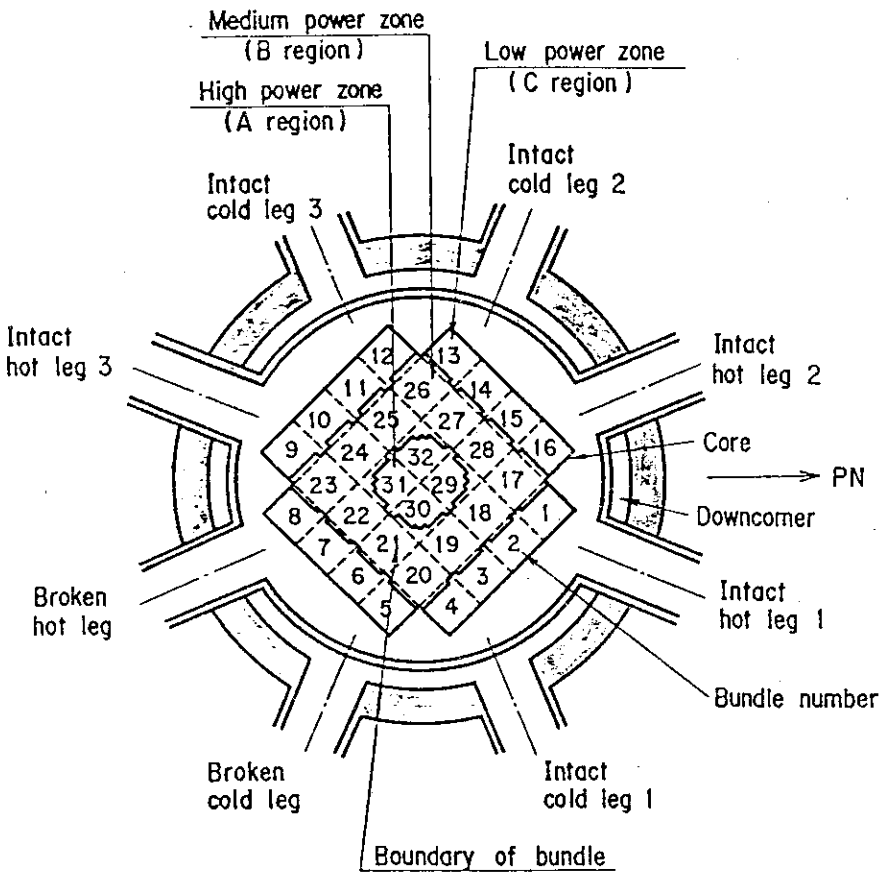

Fig. B-1 Definition of power zones and bundle numbers

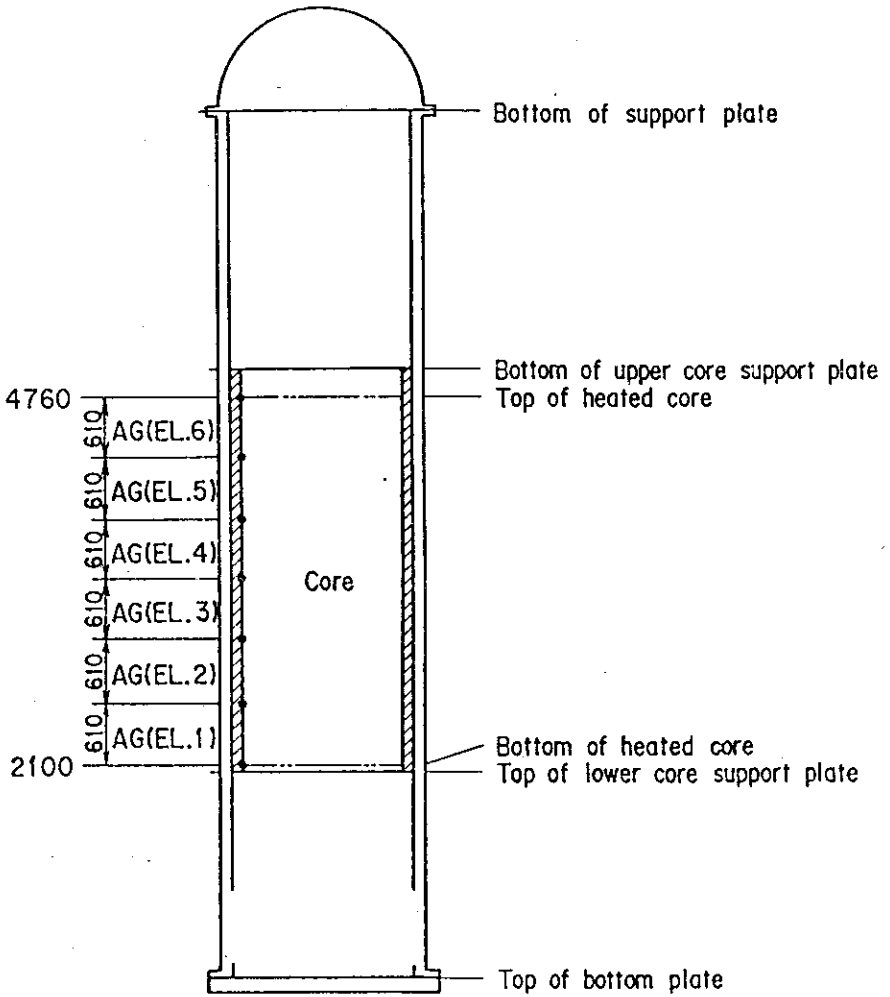

Fig. B-2 Definition of Tag.ID for void fraction (AG(EL.1) ~ AG(EL.6))

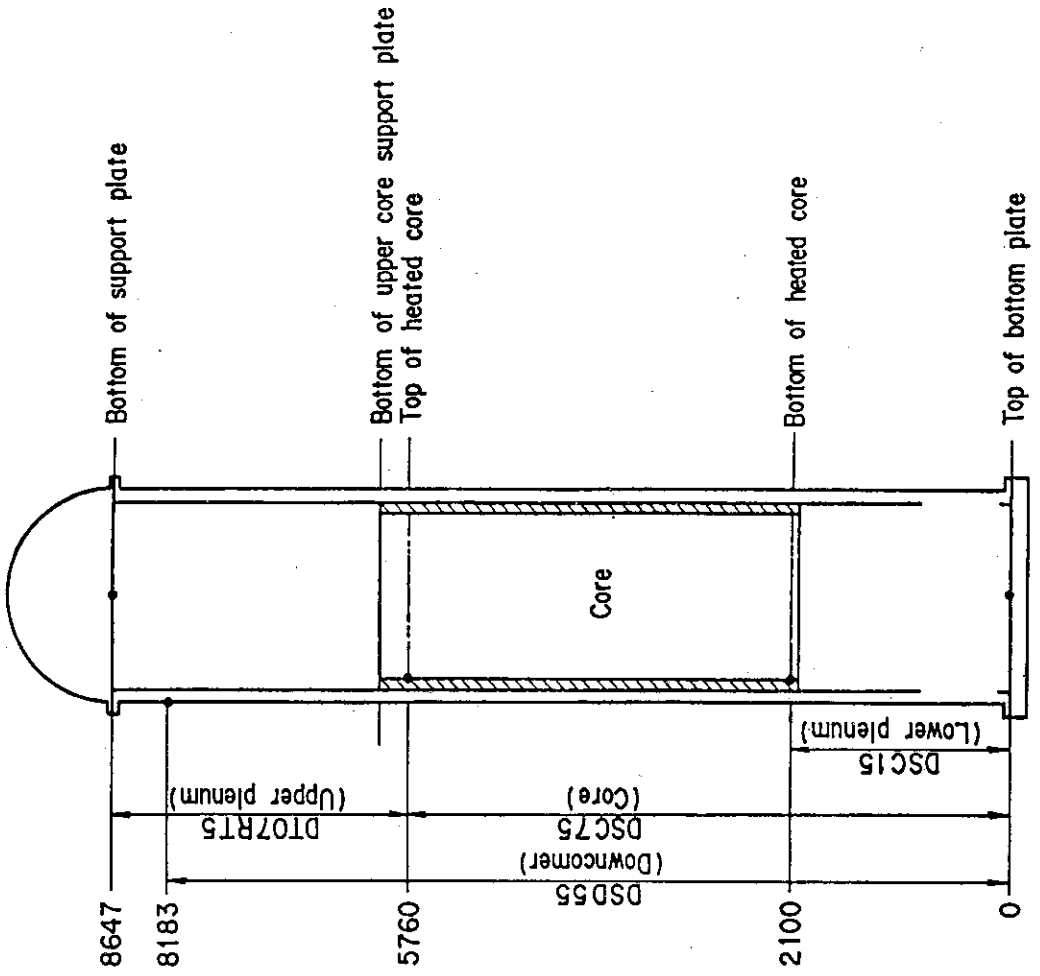

Fig. B-4 Definition of Tag.ID for differential pressure through down- comer, upper plenum, core, and lower plenum (DSD55, DTO7RT5, DSC75, DSC15)

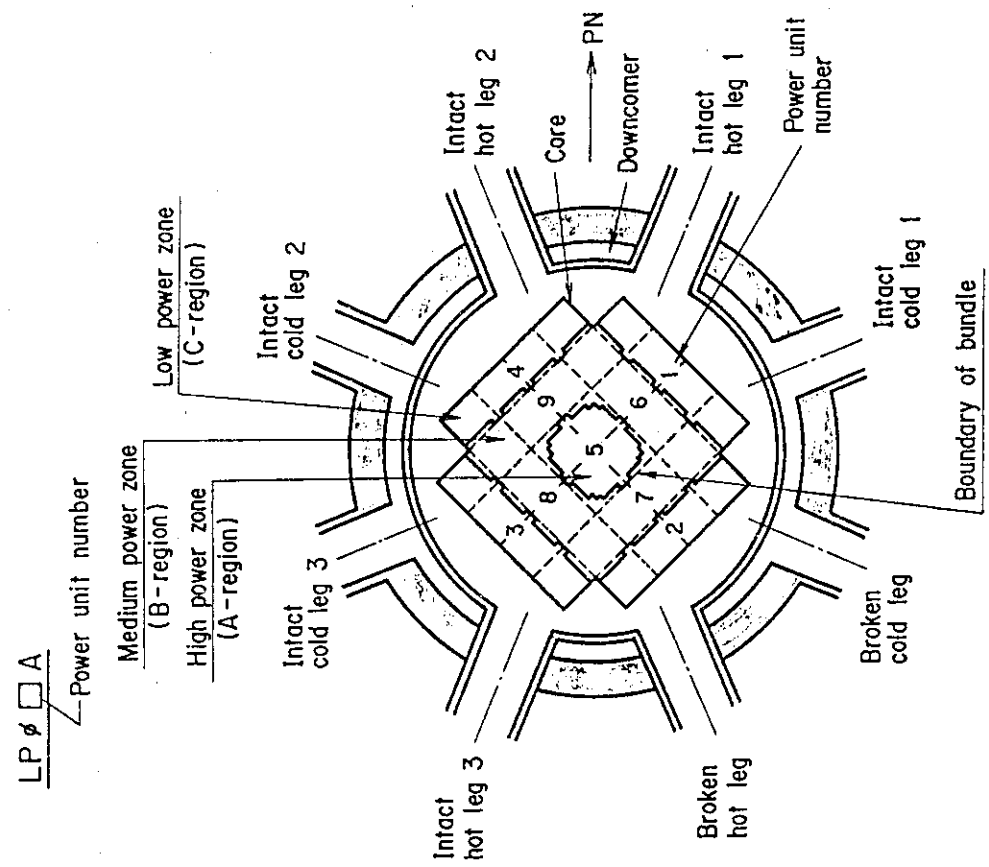

Fig. B-3 Definition of Tag.ID for average linear power of heater rod in each power unit zone (LP01A ∿ LP09A)

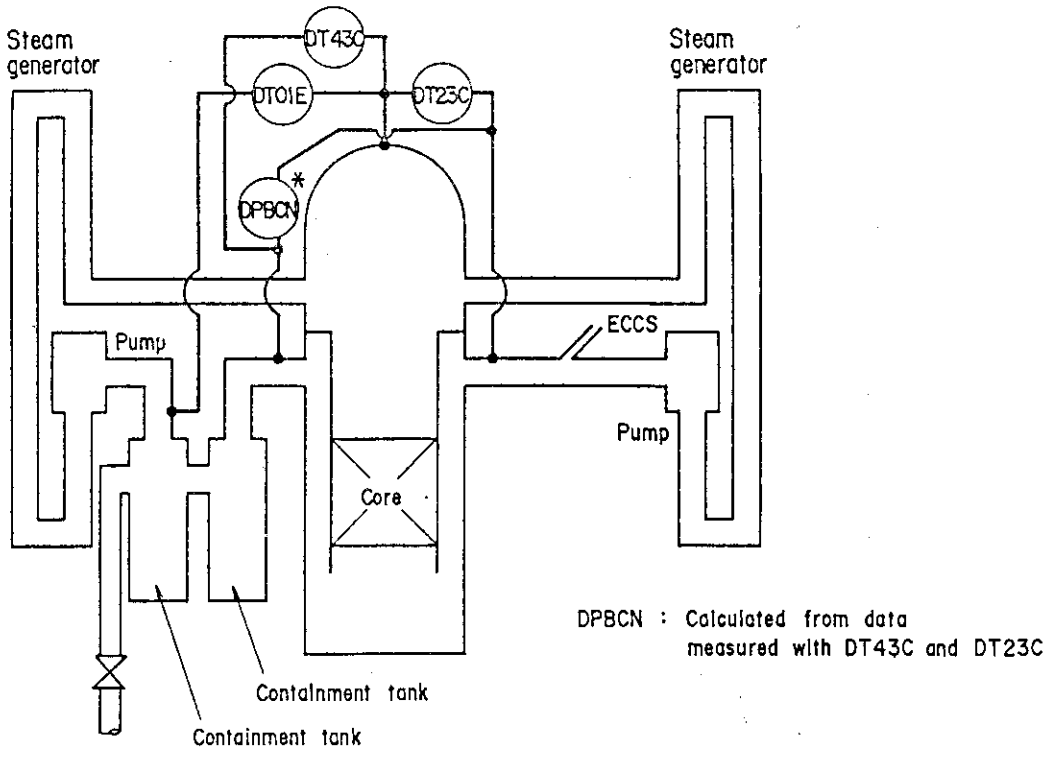

Fig. B-5 Definition of Tag.ID for differential pressure through intact and broken loop and broken cold leg nozzle (DT23C, DT01B, DPBCN)

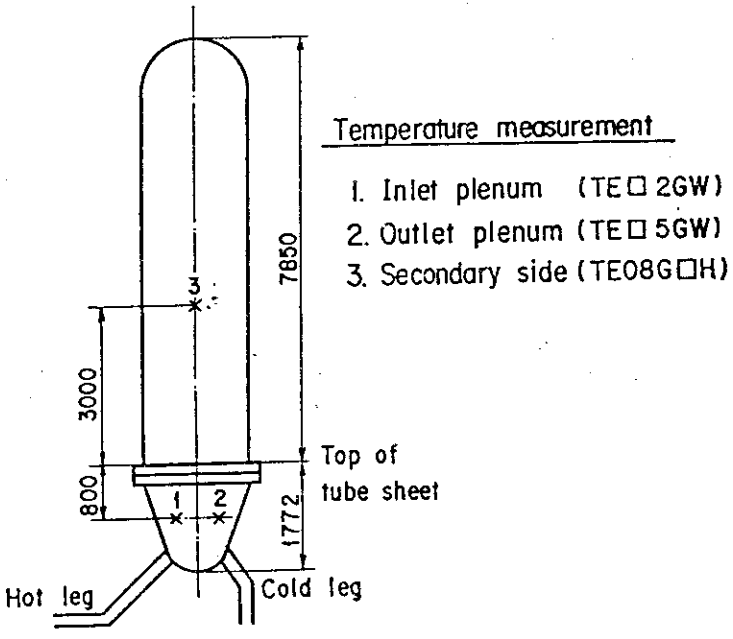

Fig. B-6 Definition of Tag.ID for fluid temperature in inlet and outlet plenum and secondary of steam generator (TE□2GW, TE□5GW, TE08G□H)

Appendix C

Main results of test C1-5 (Run 14)

Table and Figure List

Table C-1 Summary of test conditions

	Estimated	Measured
Power		
Total (MW) :	9.41	9.36
Linear (KW/m) :	1.4	1.40
Radial Power Distribution :	1.06:1.0:0.82	1.07:1.0:0.82
Decay Type : ANS x 1.2 + Actinide (30 sec after Scram)		
Pressure (kg/cm^2a)		
System :	2.0	2.02
Steam Generator Secondary :	52	50
Temperature (°C)		
Downcomer Wall :	198	182
Primary Piping Wall :	119	120
Steam Generator Secondary :	265	262
Peak Clad at ECC Initiation :	502	502
Peak Clad at BOCREC :	600	615
Lower Plenum Filled Liquid :	119	114
ECC Liquid :	35	39
Water Level (m)		
Lower Plenum :	0.9	0.87
Steam Generator Secondary :	7.4	7.3
Injection Rate (m^3/hr)		
Accumlator :	251	278
LPCI :	30	30.2

Table C-2 Chronology of events

EVENT	TIME (sec)
Test C1-5 initiated (Heater rods power on) (Data recording initiated)	0.0
Accumulator injection initiated	52.5
Power decay initiated (Bottom of core recovery)	63
Accumulator injection switched from lower plenum to cold leg	67
Accumulator injection ended and LPCI injection initiated	76
All heater rods quenched	598
Power off	648
LPCI injection ended	738
Test ended (Data recording ended)	1068

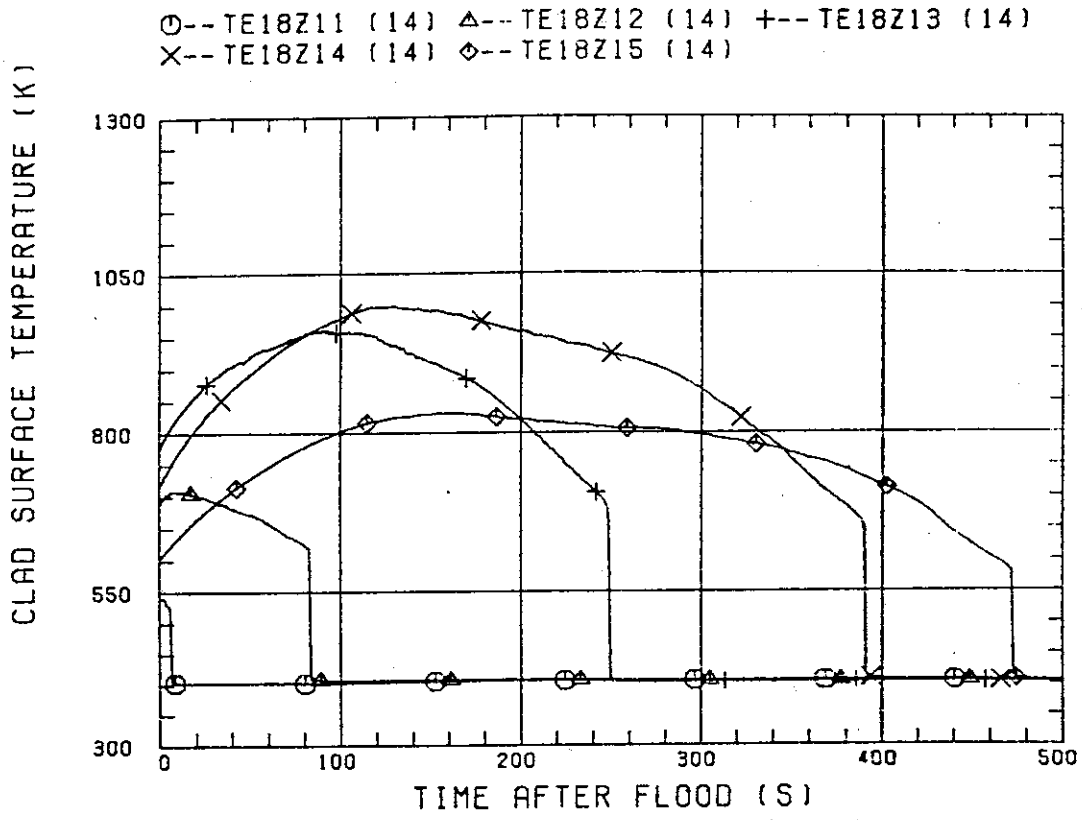

Fig. C-1 Surface temperature on low power rod (Z-rod) in medium power region (B region) (average power rod)

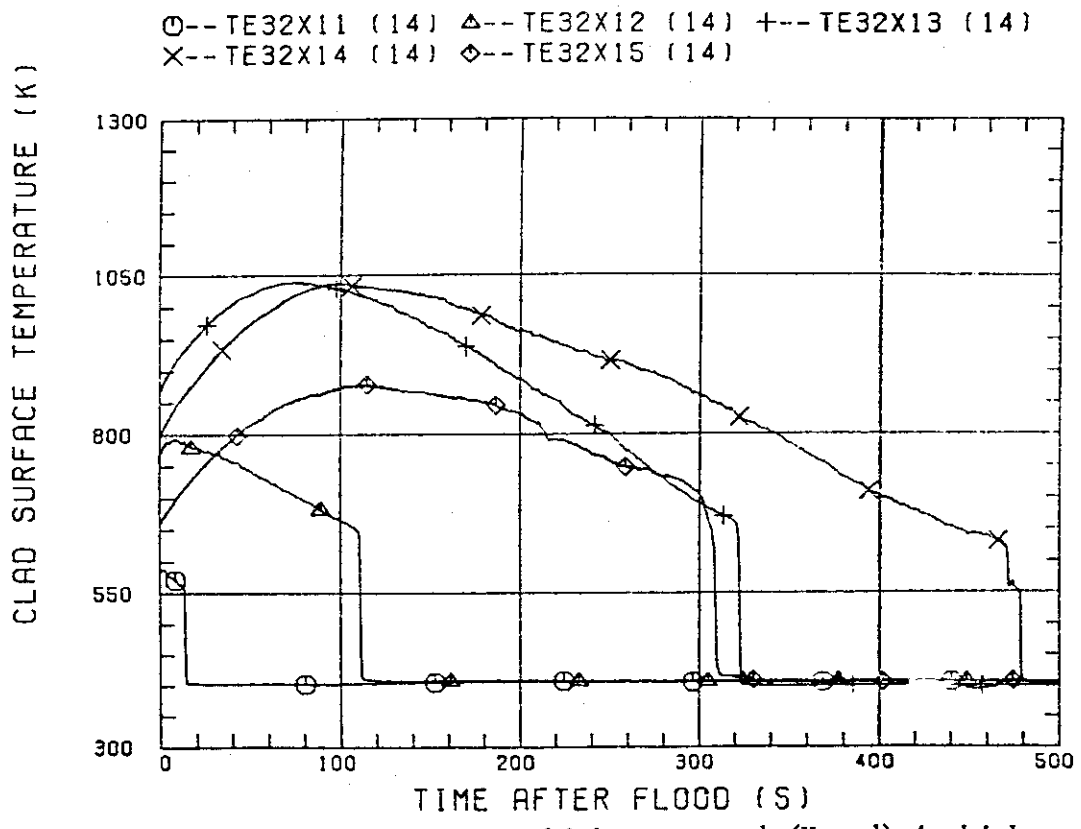

Fig. C-2 Surface temperature on high power rod (X-rod) in high power region (A region) (peak power rod)

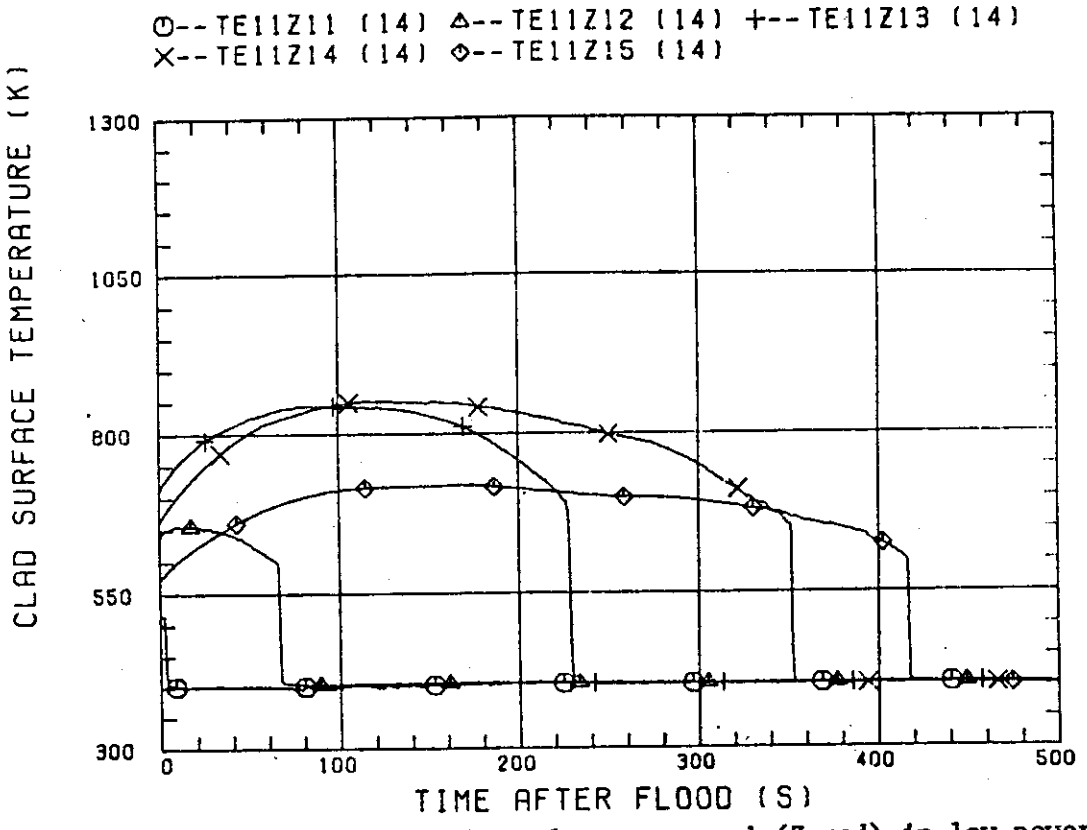

Fig. C-3 **Surface temperature on low power rod (Z-rod) in low power region (C region) (lowest power rod)**

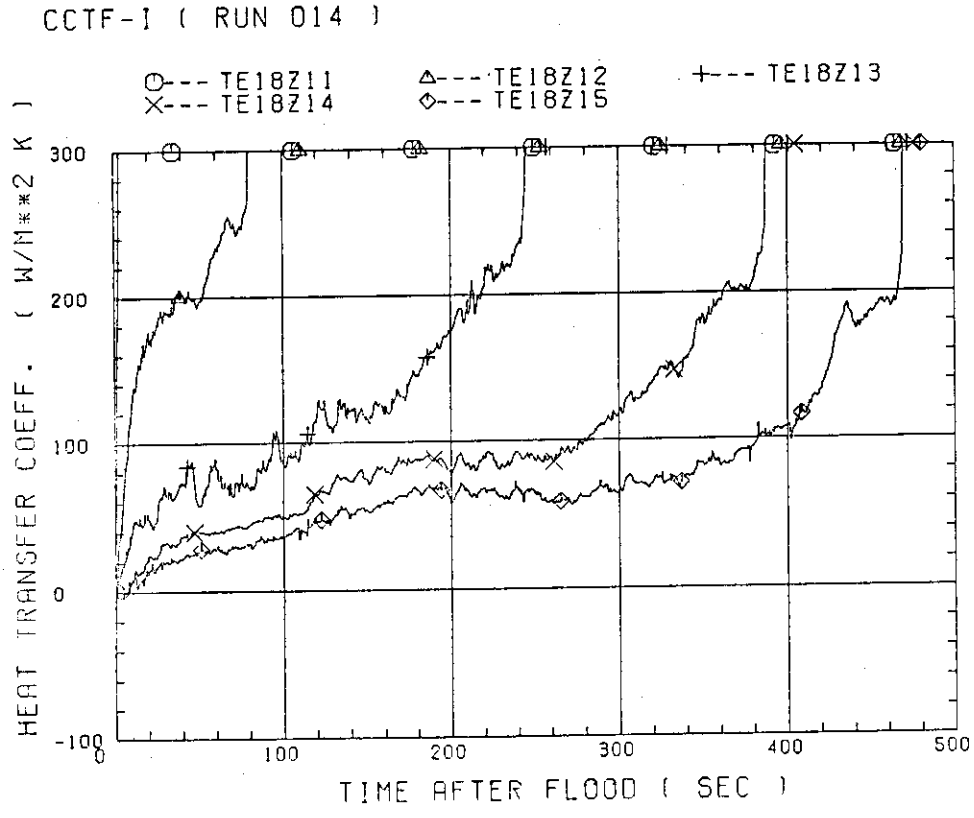

Fig. C-4 **Heat transfer coefficient at midplane of low power rod (Z-rod) in medium power region (B region) (average power rod)**

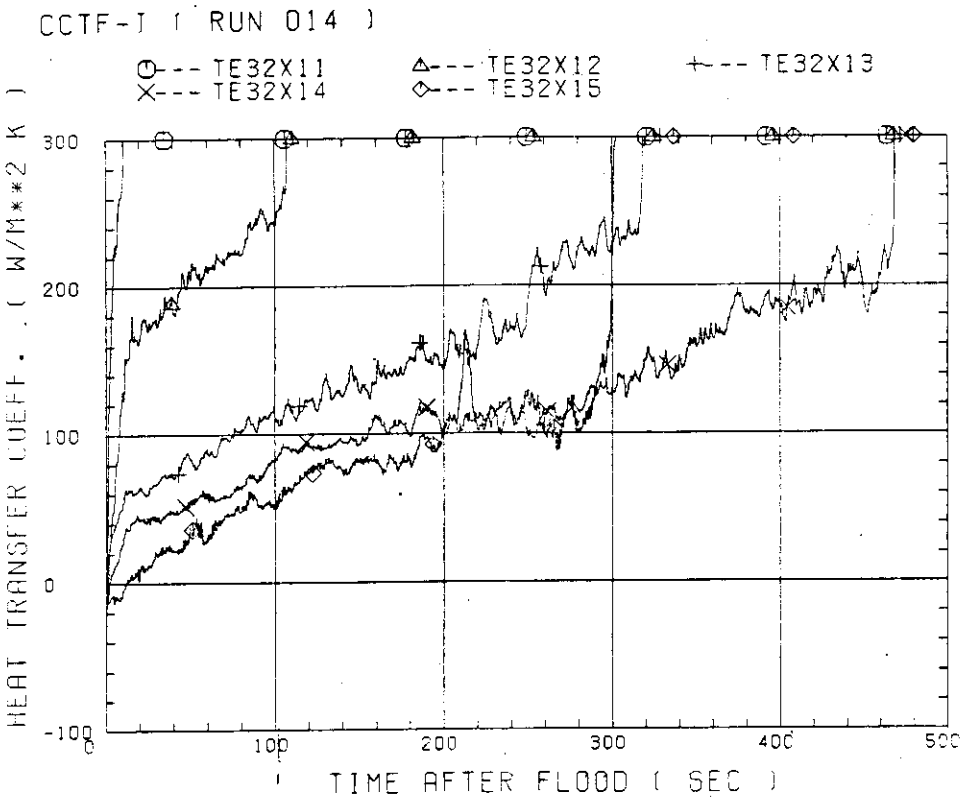

Fig. C-5 Heat transfer coefficient at midplane of high power rod (X-rod) in high power region (A region) (peak power rod)

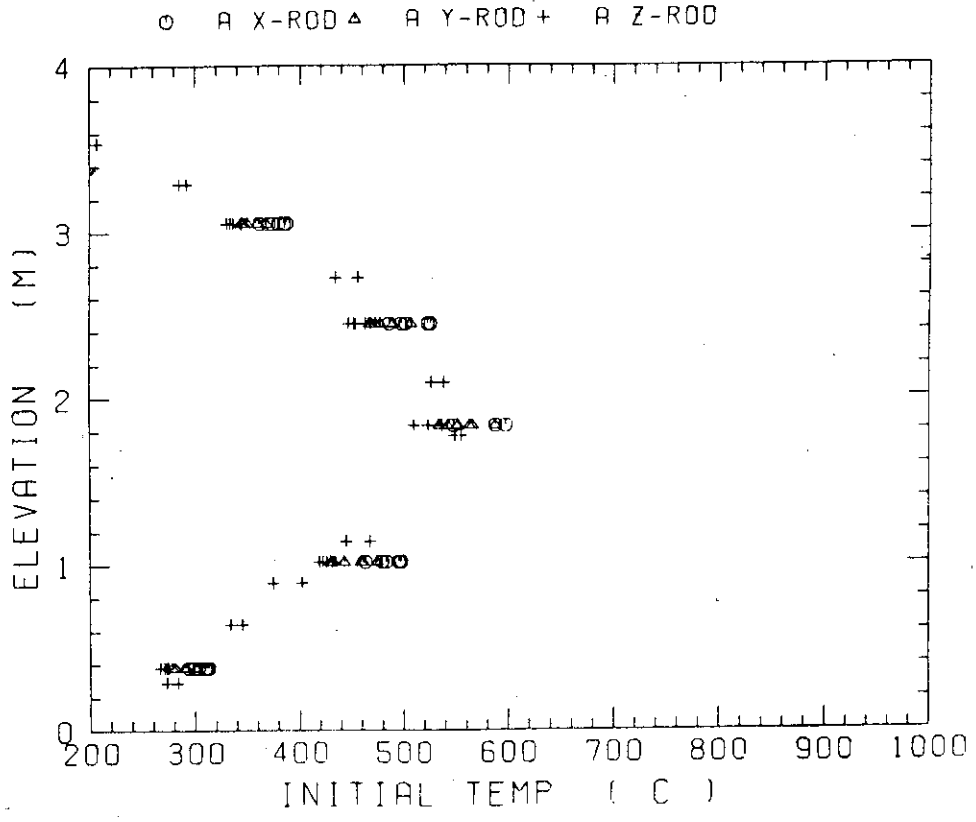

Fig. C-6 Initial rod surface temperature in high power region (A region)

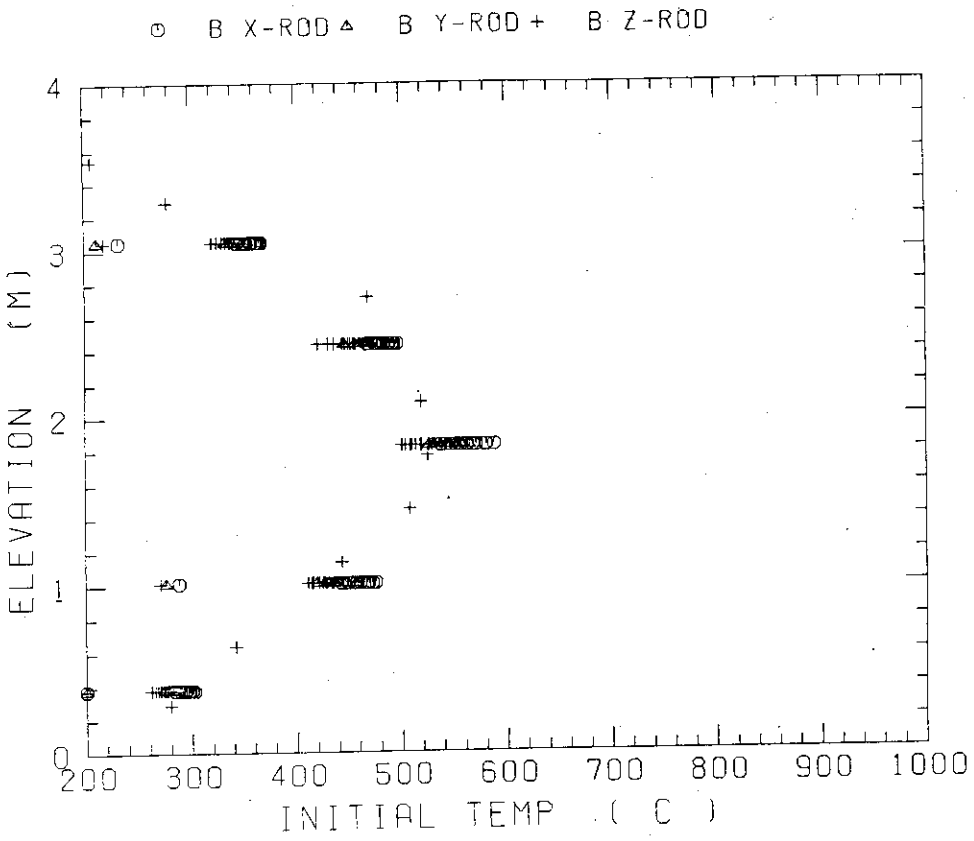

Fig. C-7 Initial rod surface temperature in medium power region (B region)

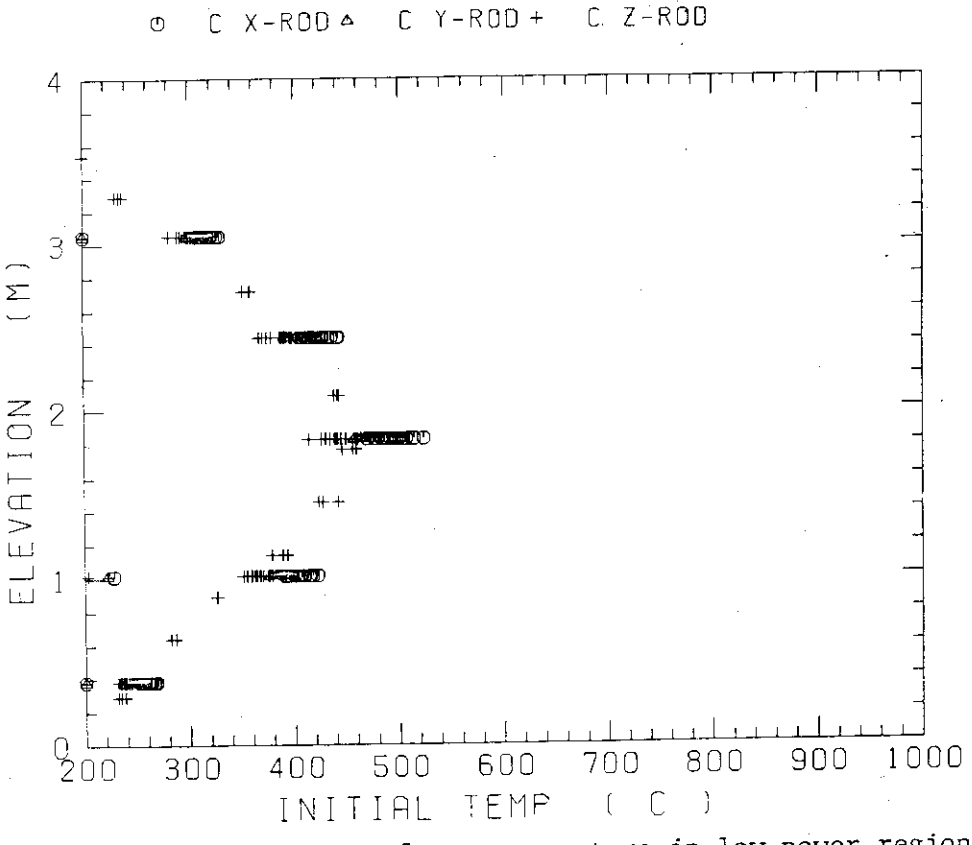

Fig. C-8 Initial rod surface temperature in low power region (C region)

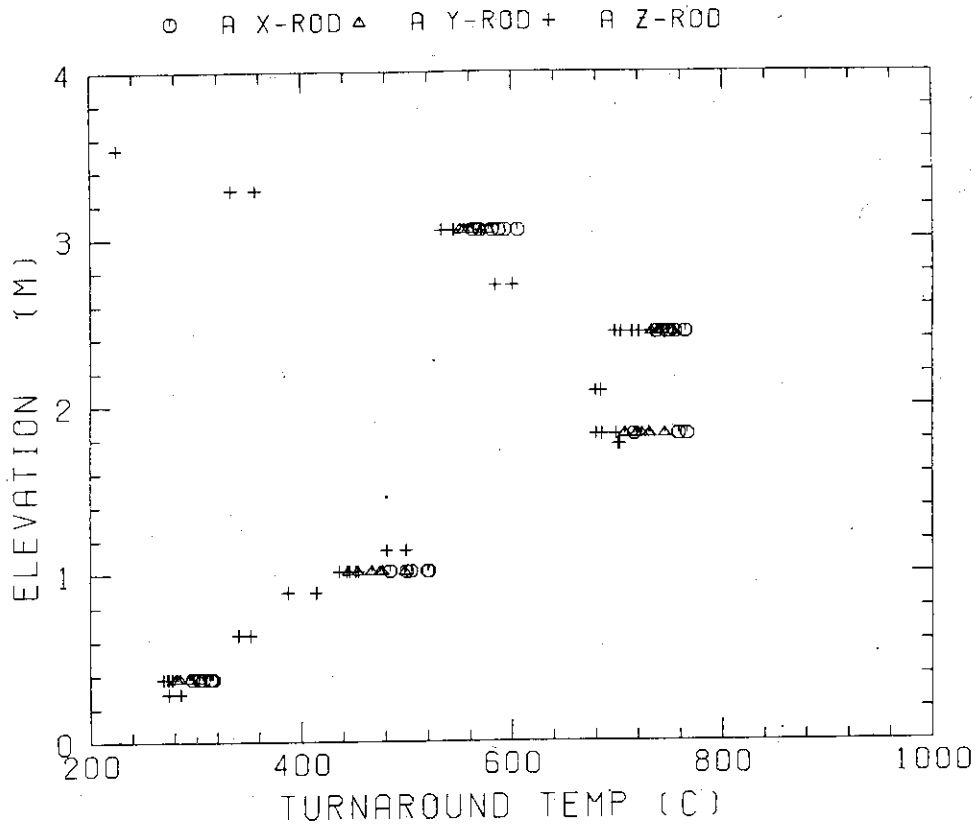

Fig. C-9 Turnaround temperature in high power region (A region)

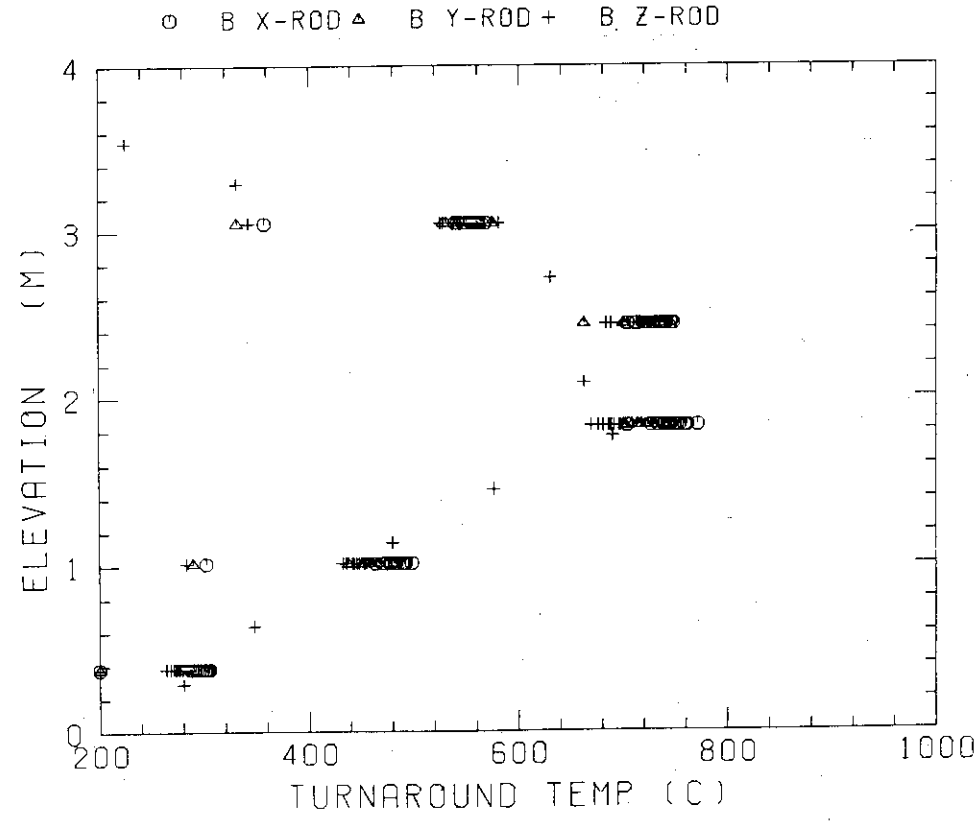

Fig. C-10 Turnaround temperature in medium power region (B region)

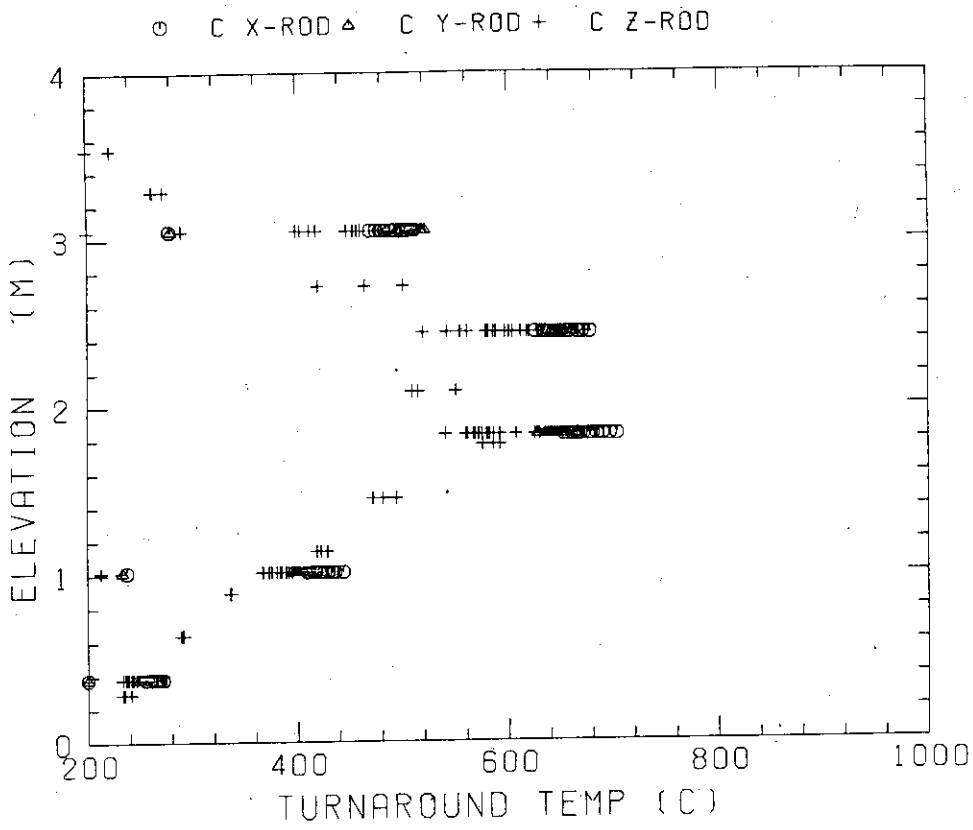

Fig. C-11 Turnaround temperature in low power region (C region)

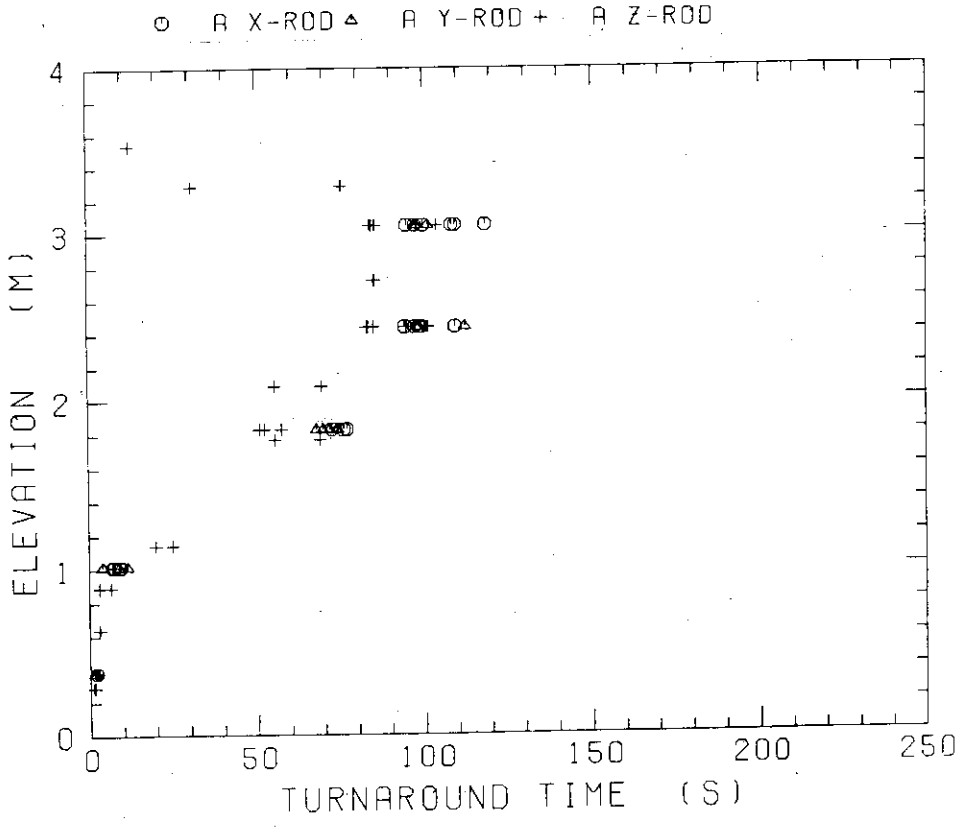

Fig. C-12 Turnaround time in high power region (A region)

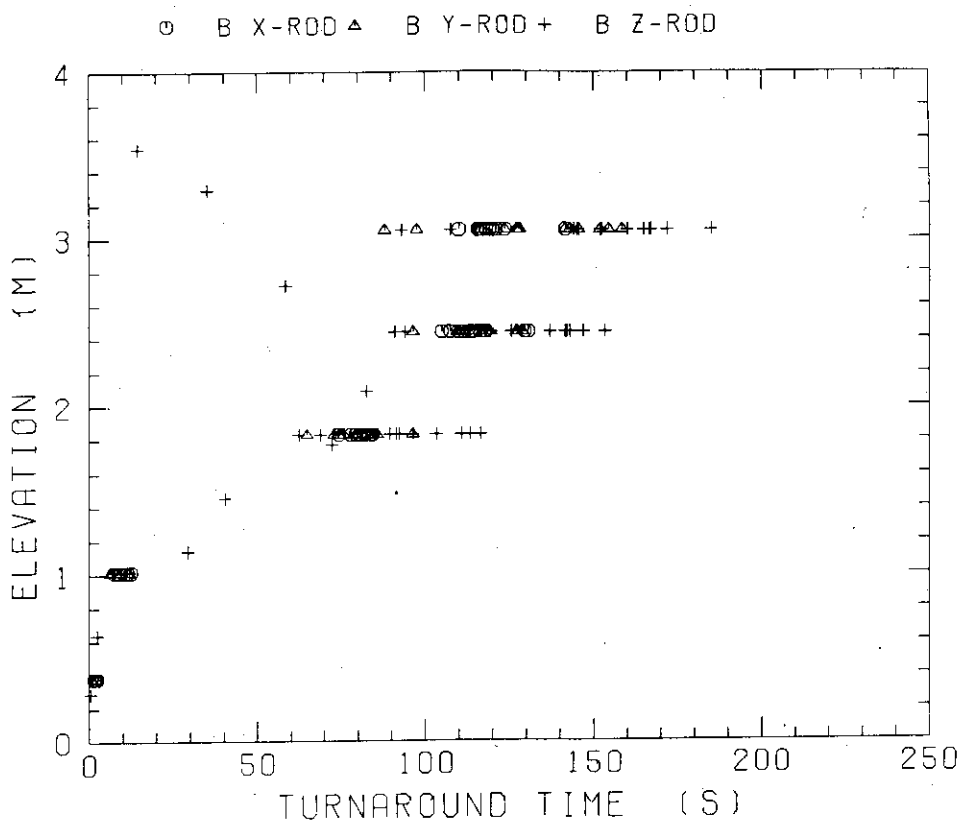

Fig. C-13 Turnaround time in medium power region (B region)

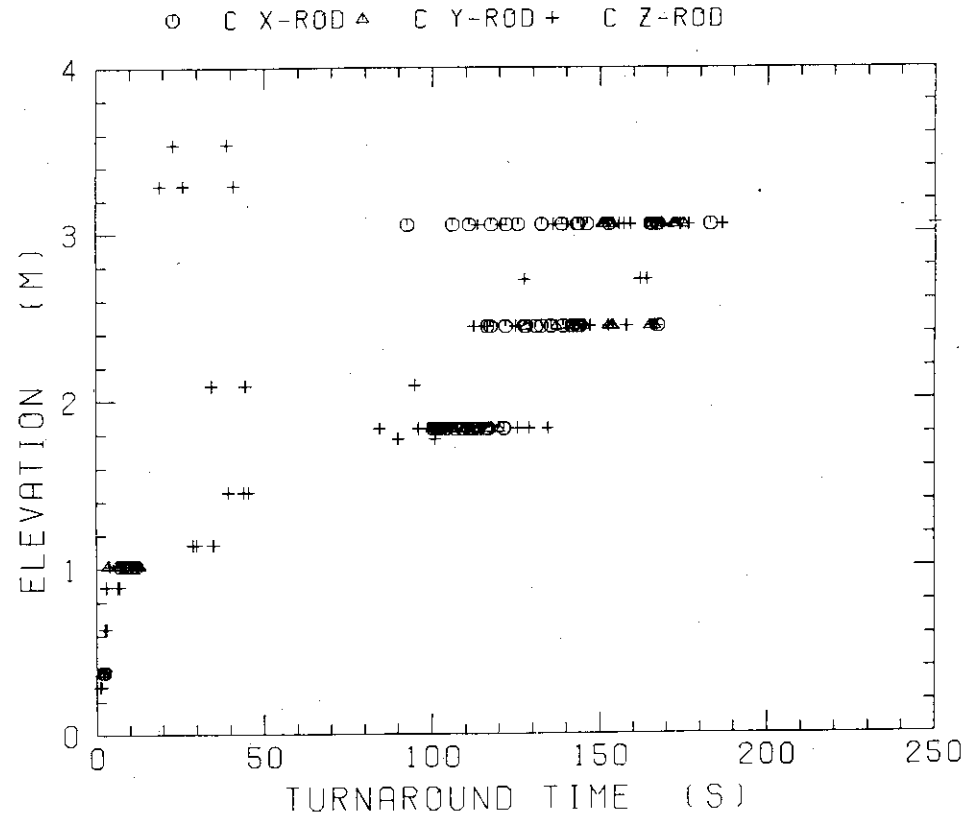

Fig. C-14 Turnaround time in low power region (C region)

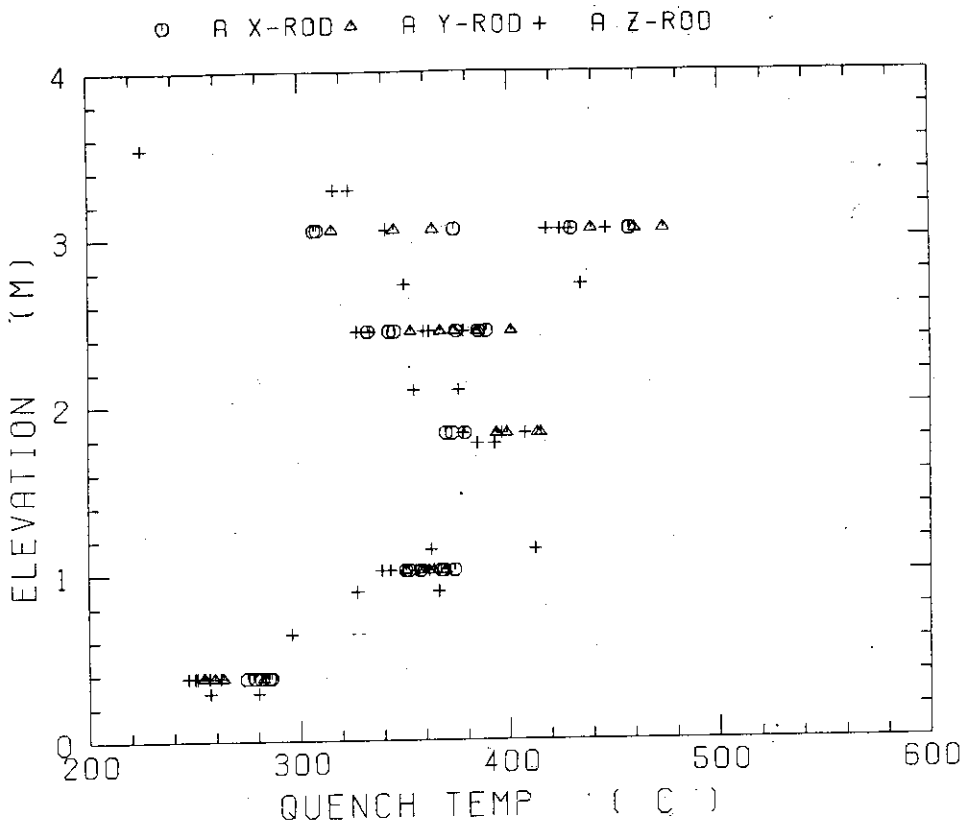

Fig. C-15 Quench temperature in high power region (A region)

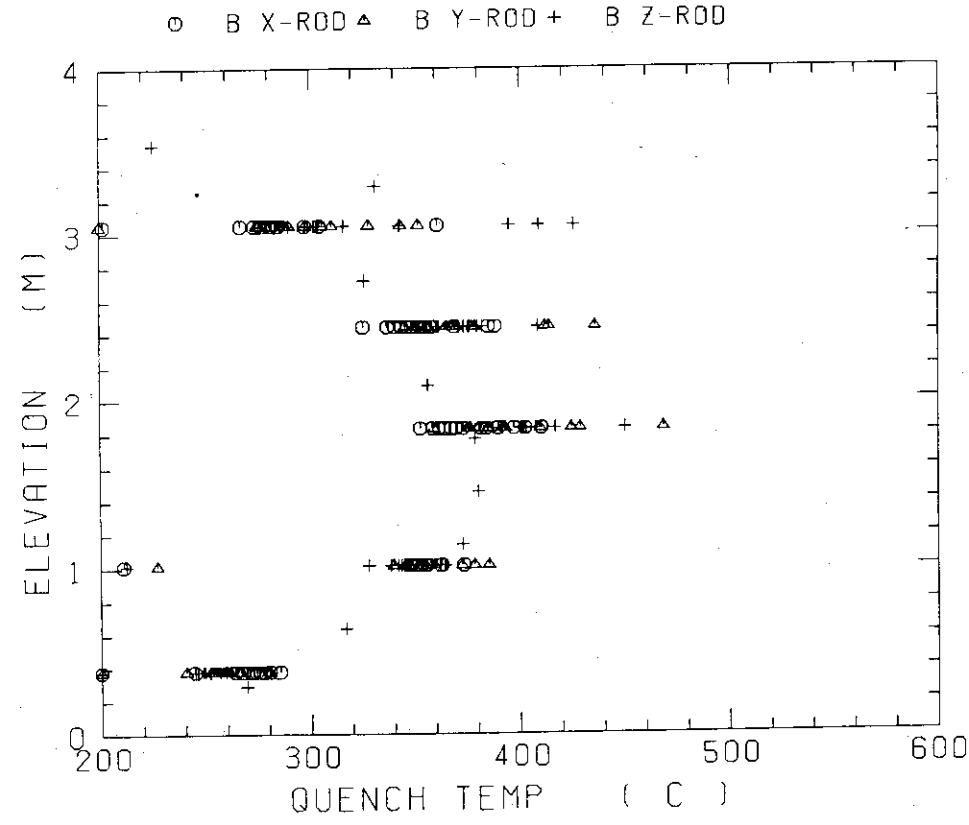

Fig. C-16 Quench temperature in medium power region (B region)

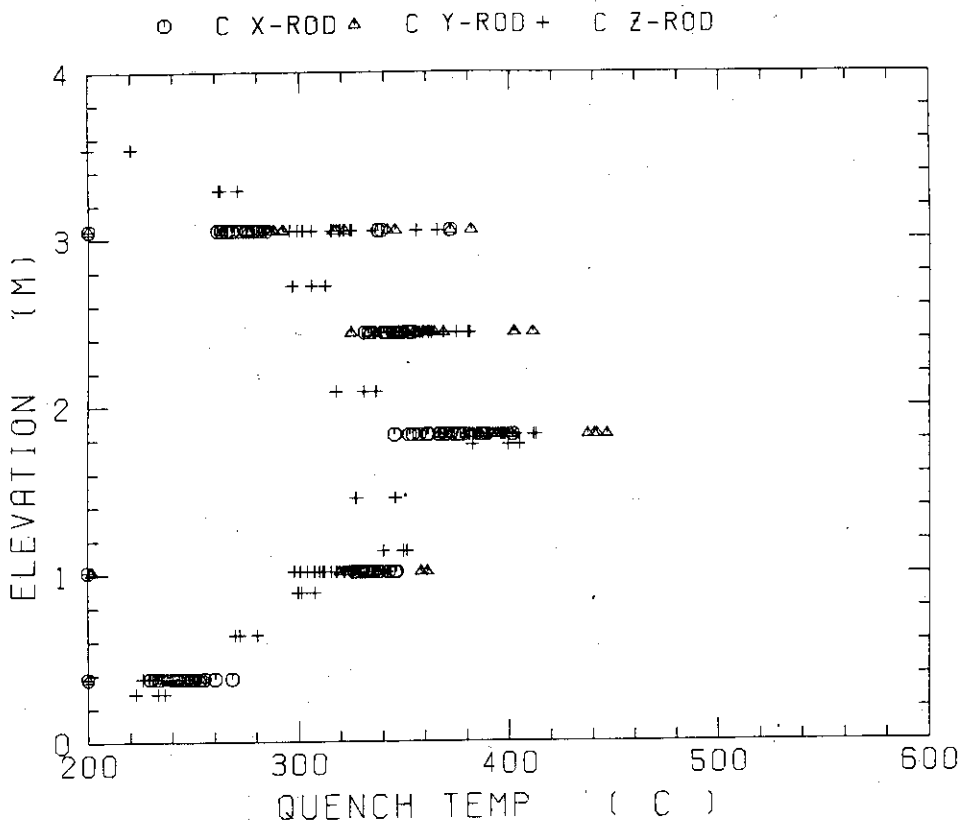

Fig. C-17 Quench temperature in low power region (C region)

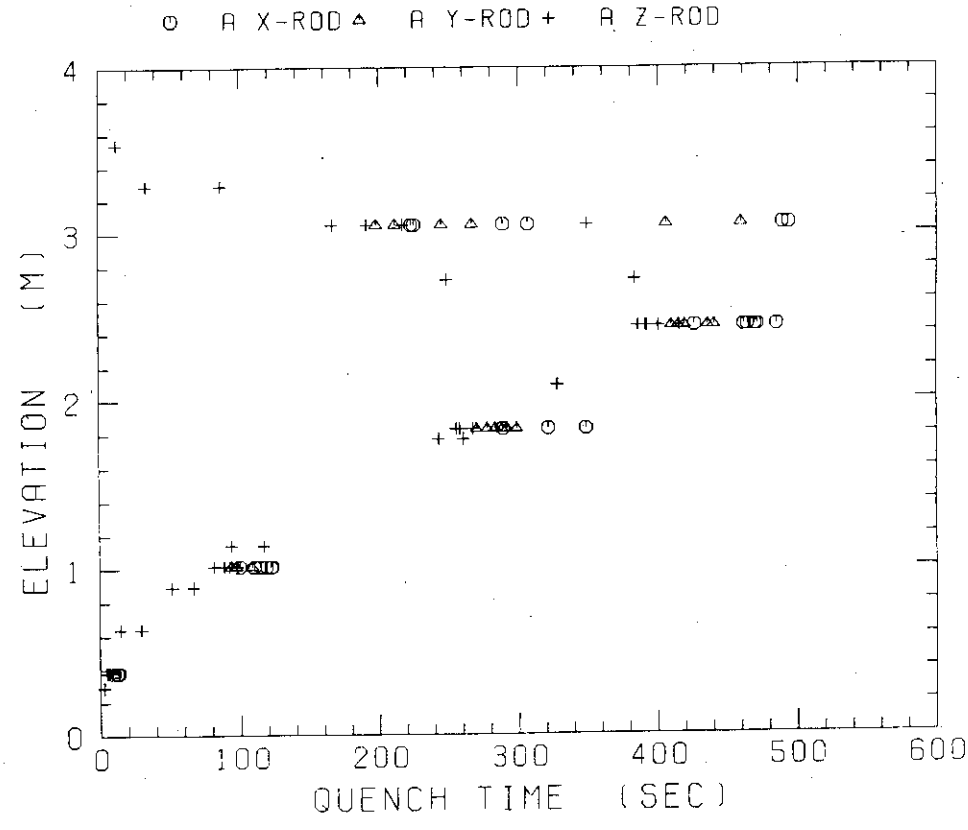

Fig. C-18 Quench time in high power region (A region)

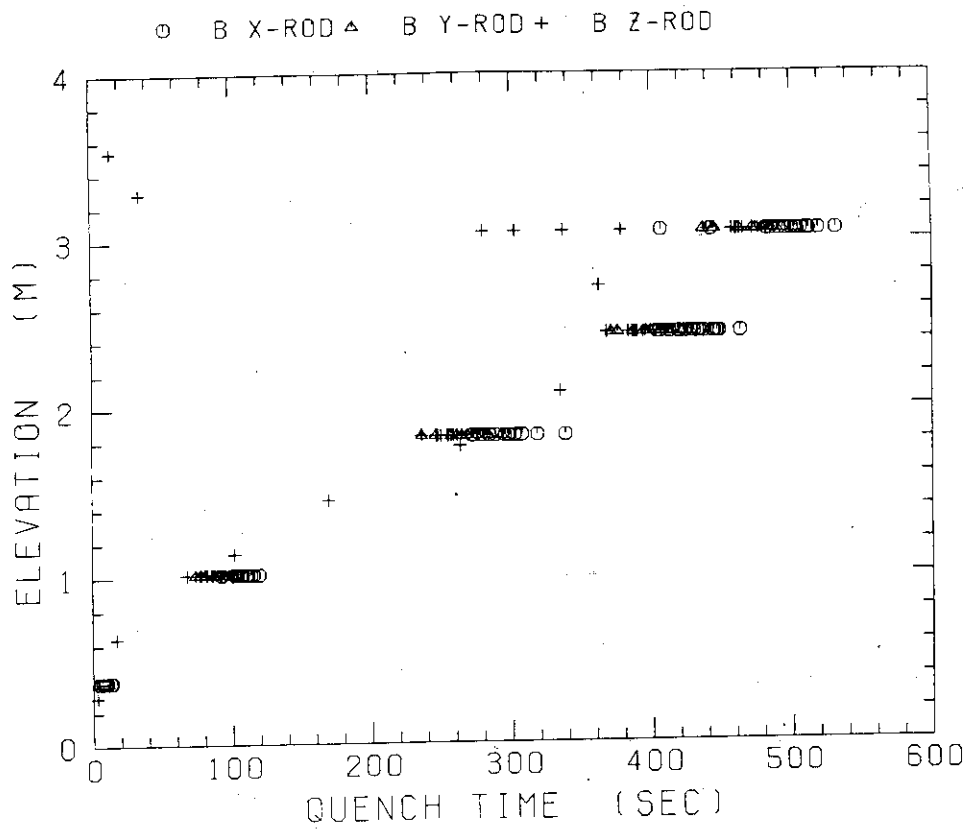

Fig. C-19 Quench time in medium power region (B region)

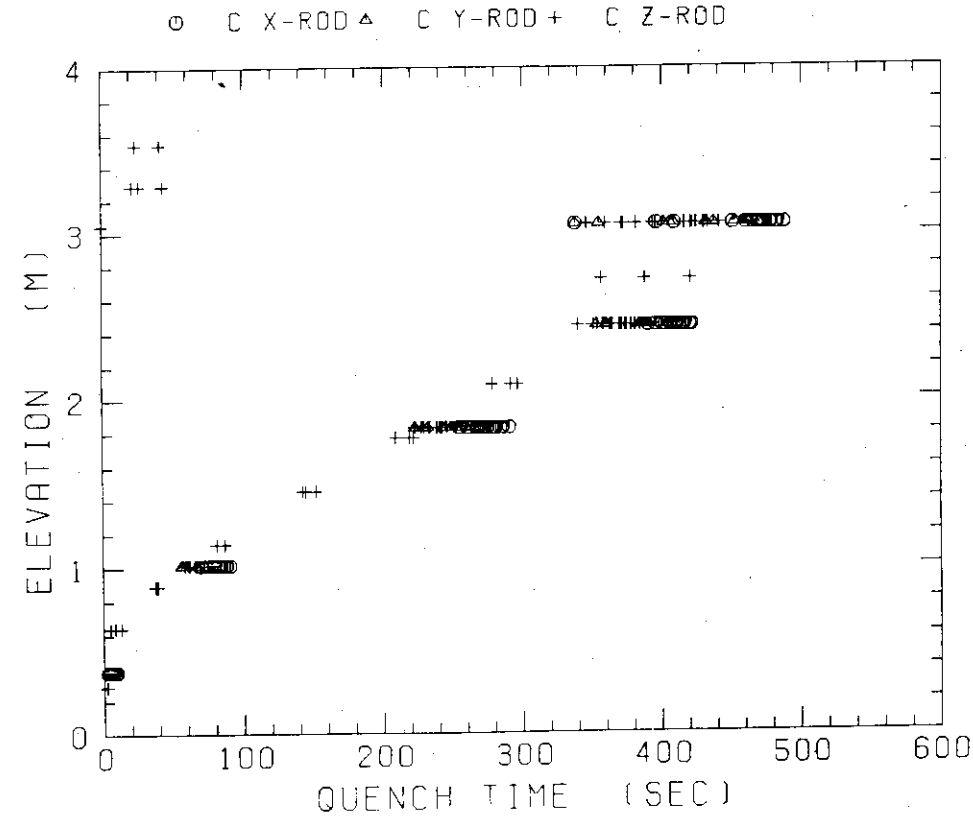

Fig. C-20 Quench time in low power region (C region)

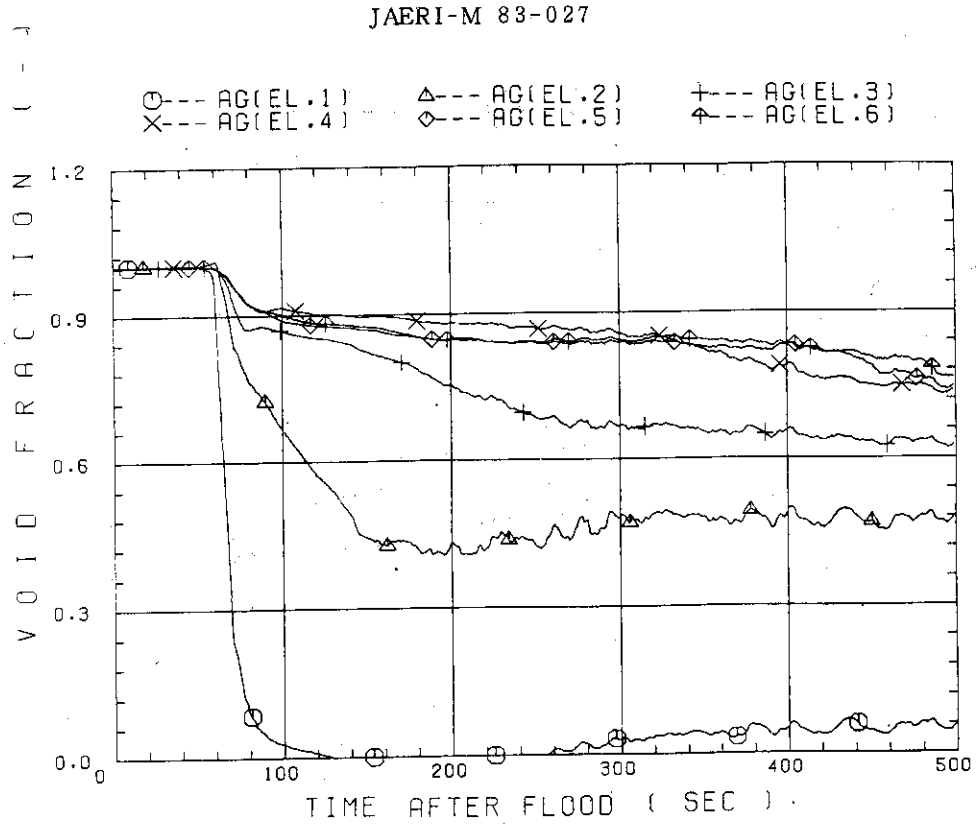

Fig. C-21 Void fraction in core

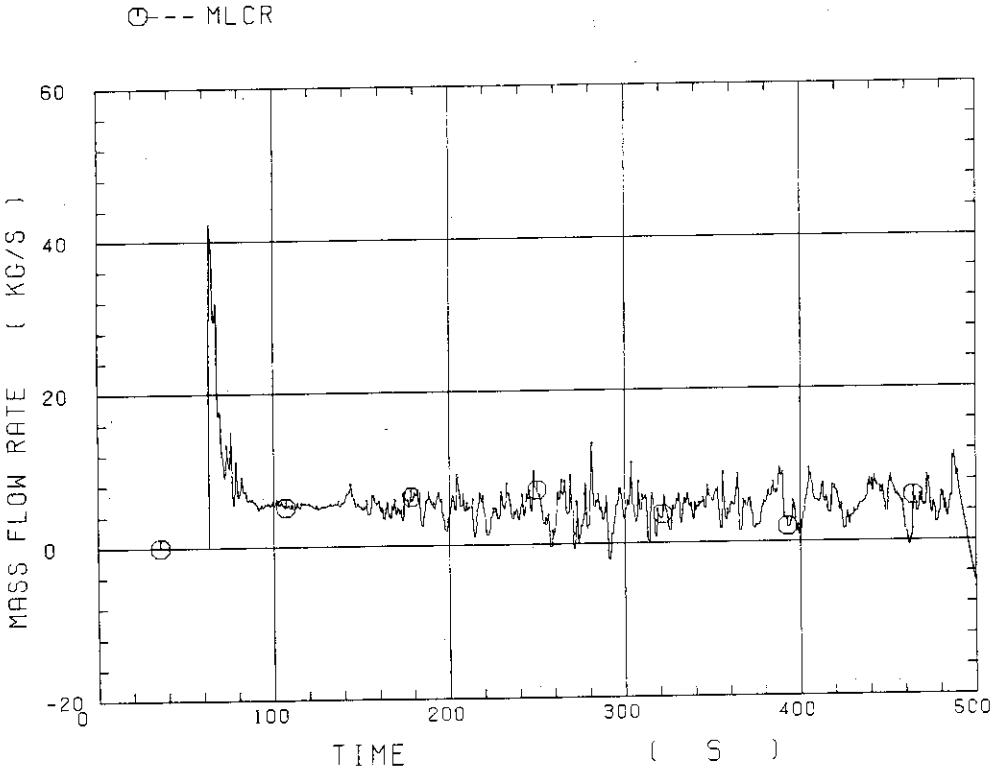

Fig. C-22 Core inlet mass flow rate

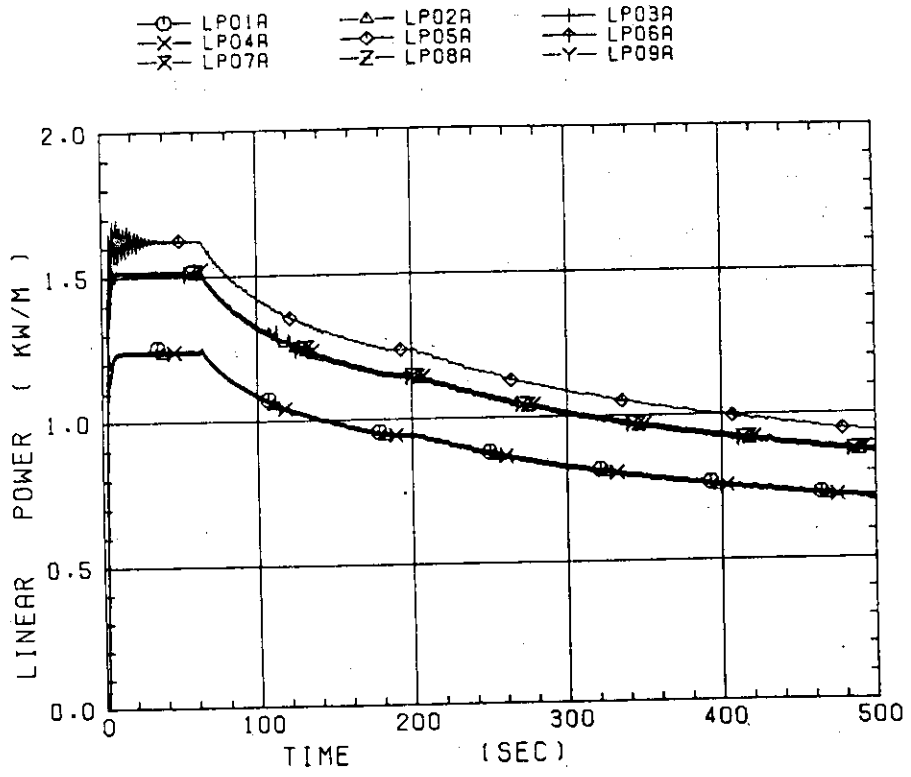

Fig. C-23 Average linear power of heater rod in each power unit zone

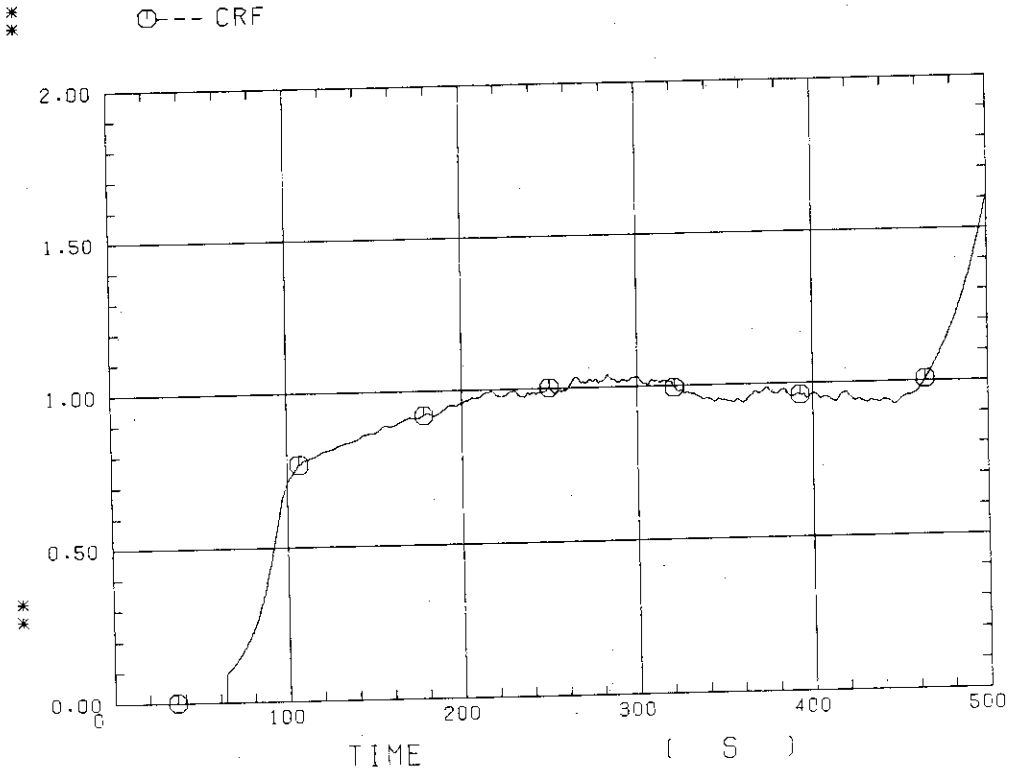

Fig. C-24 Carry-over rate fraction

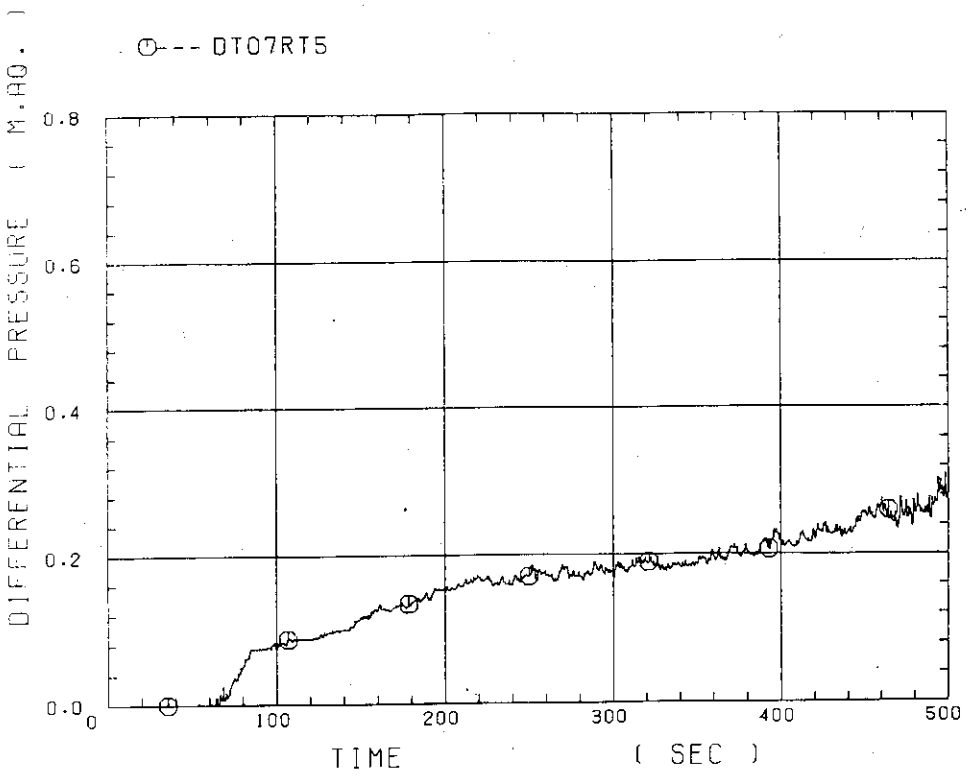

Fig. C-25 Differential pressure through upper plenum

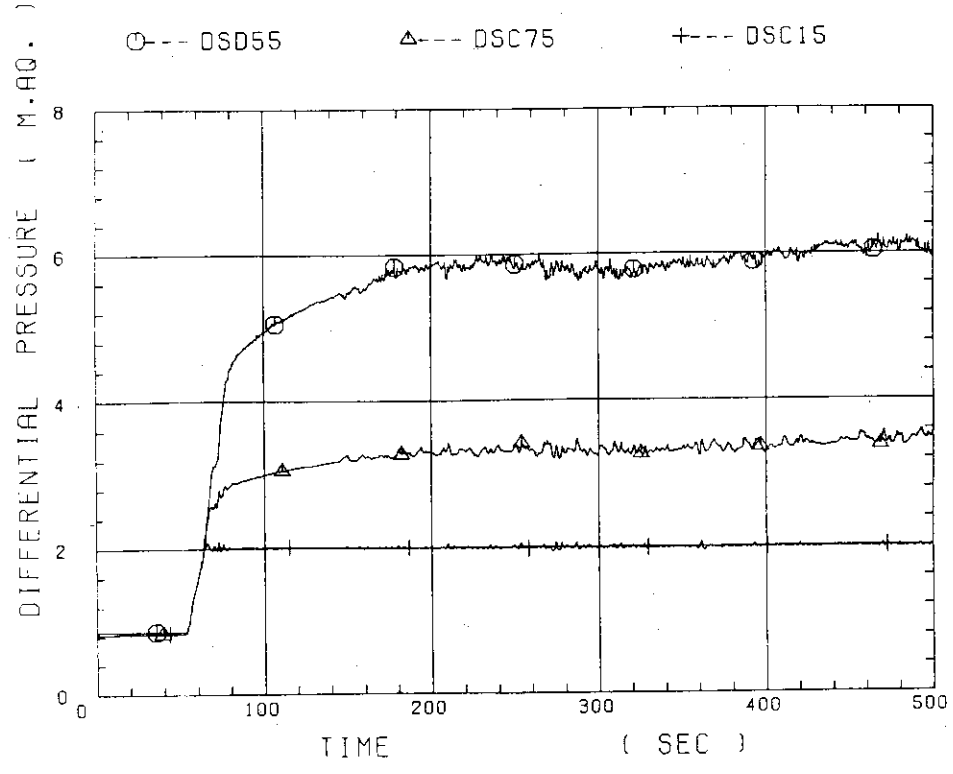

Fig. C-26 Differential pressure through downcomer, core, and lower plenum

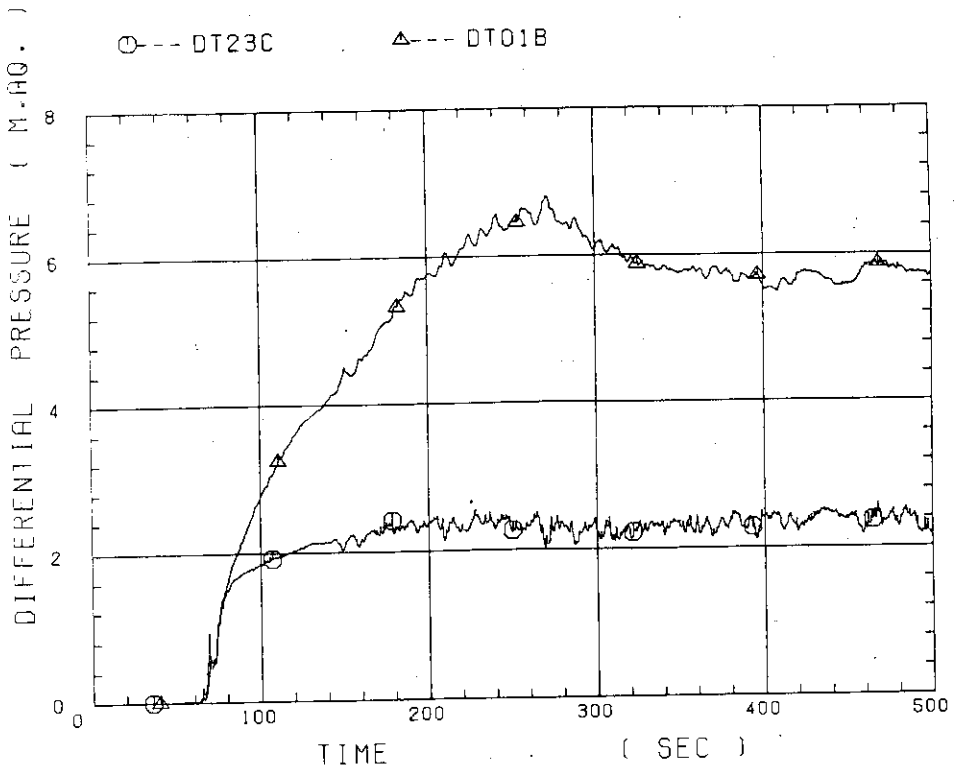

Fig. C-27 Differential pressure through intact and broken loops

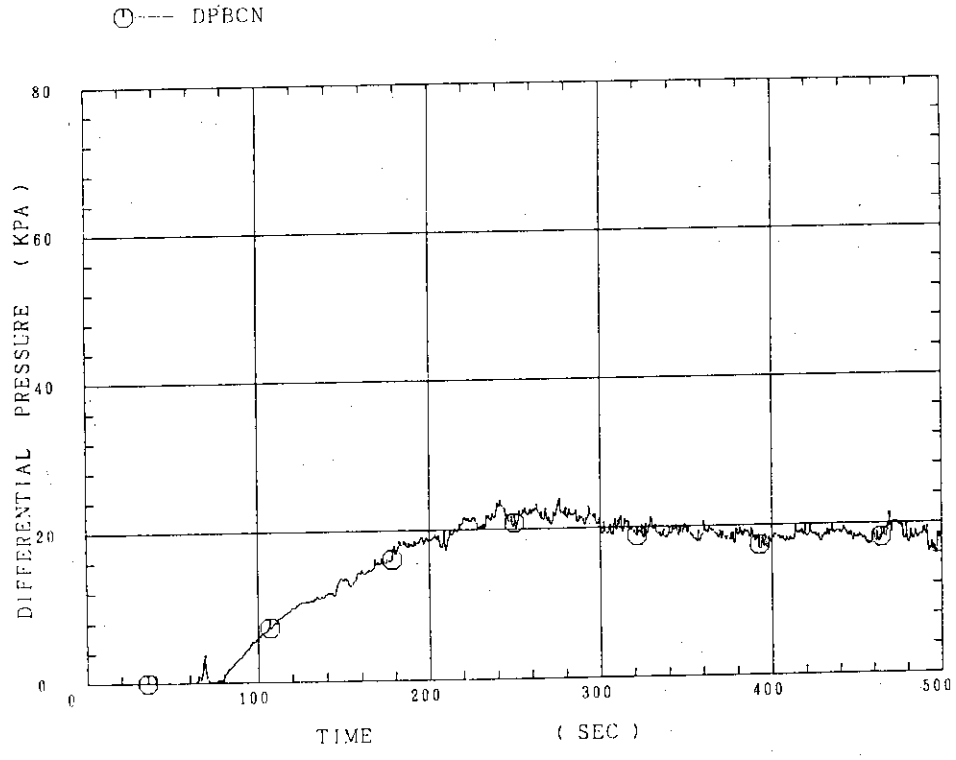

Fig. C-28 Differential pressure through broken cold leg nozzle

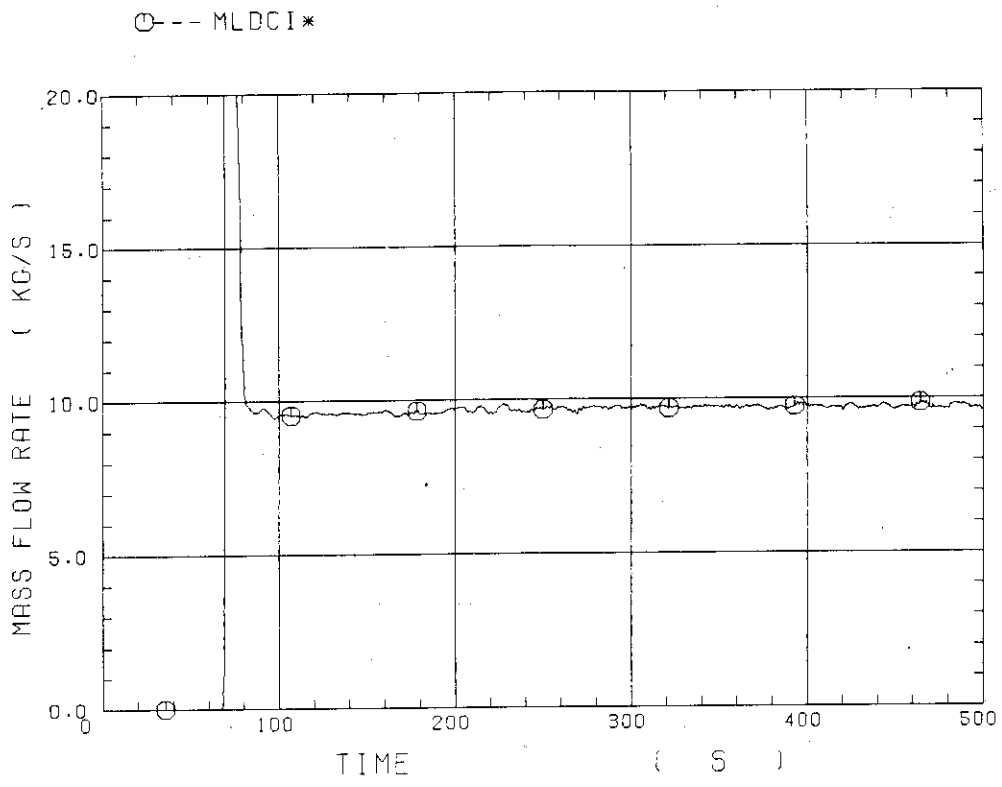

Fig. C-29 Total water mass flow rate from intact loops to downcomer

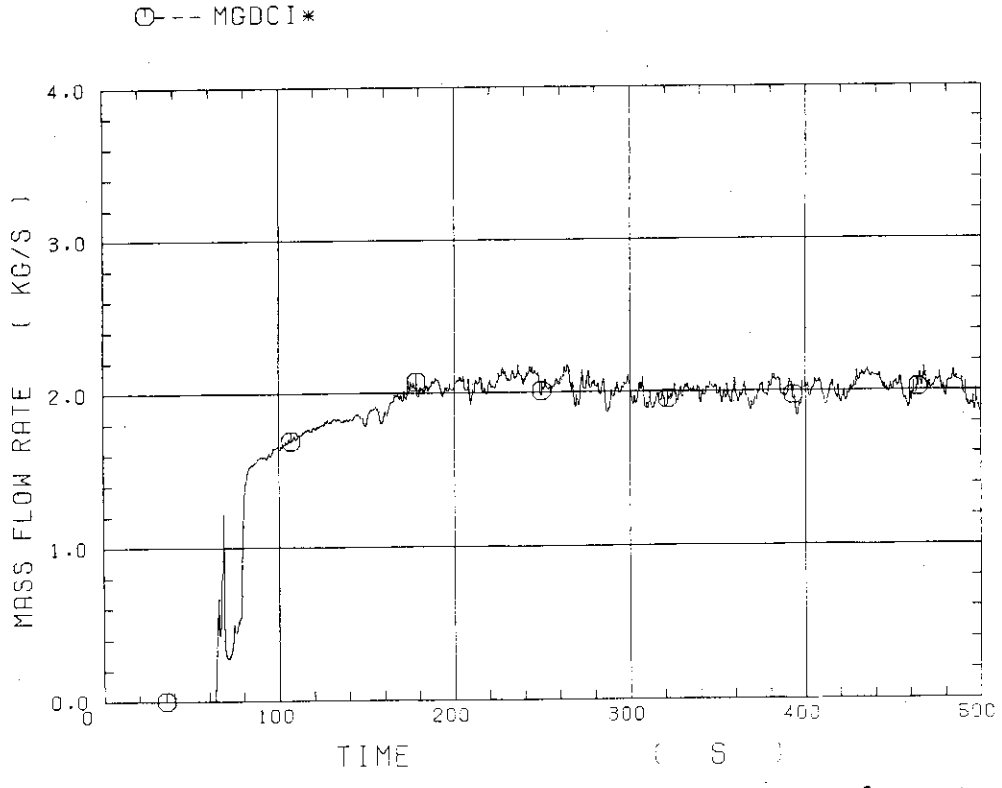

Fig. C-30 Total steam mass flow rate from intact loops to downcomer

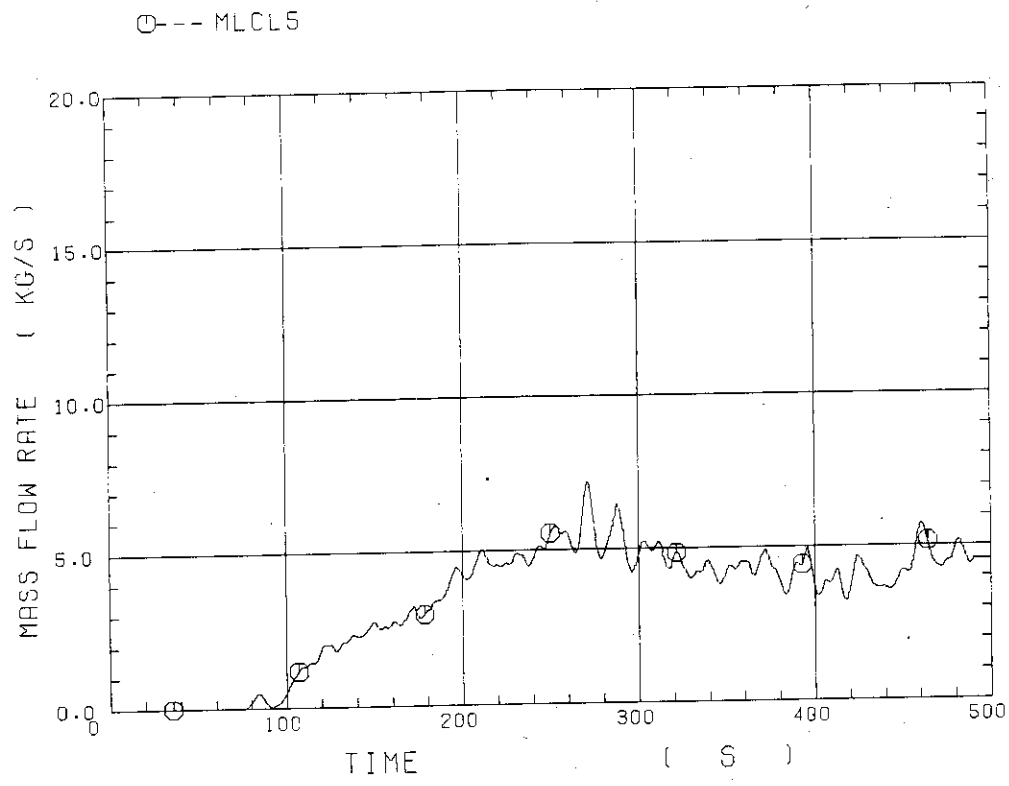

Fig. C-31 Water mass flow rate through broken cold leg nozzle

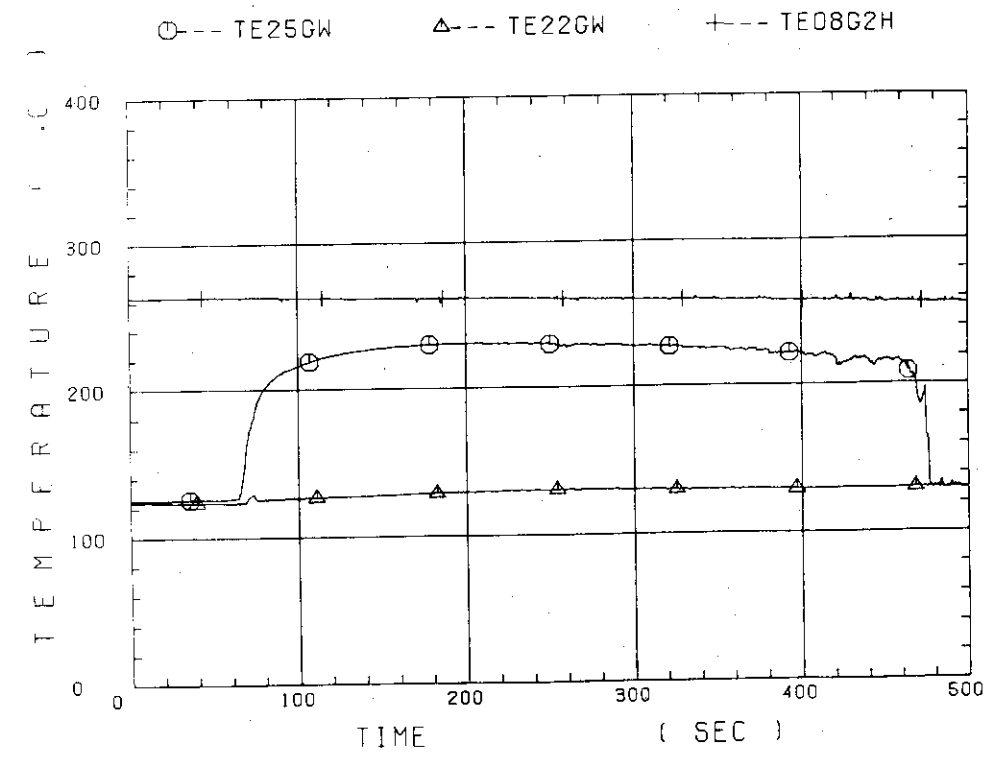

Fig. C-32 Fluid temperature in inlet plenum, outlet plenum, and secondary of steam generator 1

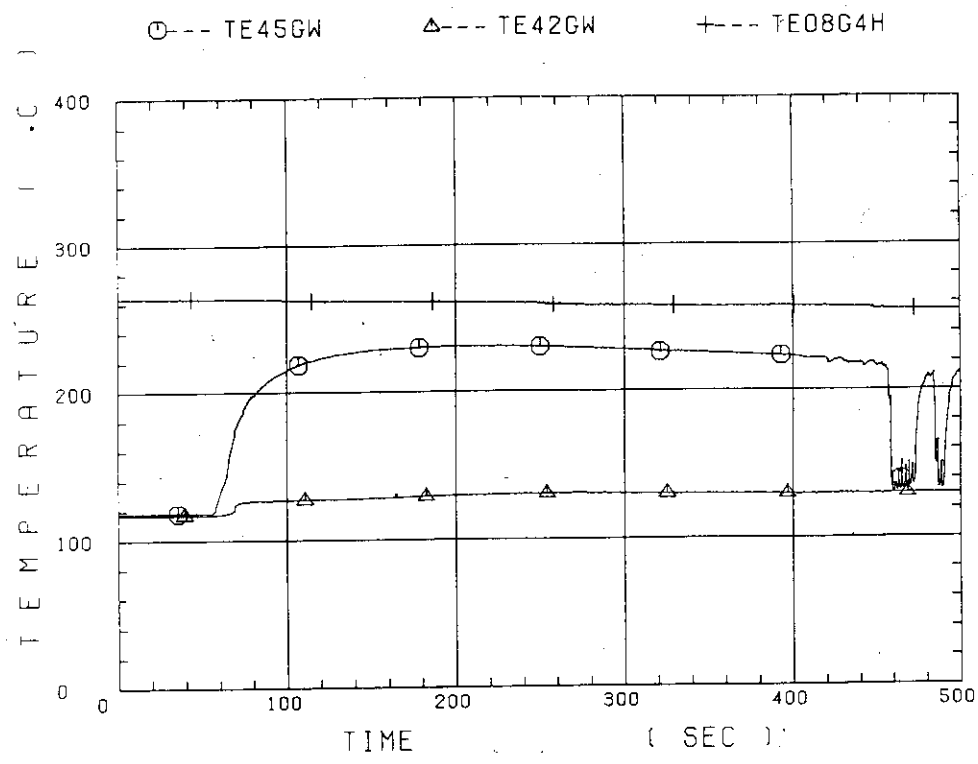

Fig. C-33 Fluid temperature in inlet plenum, output plenum, and secondary of steam generator 2

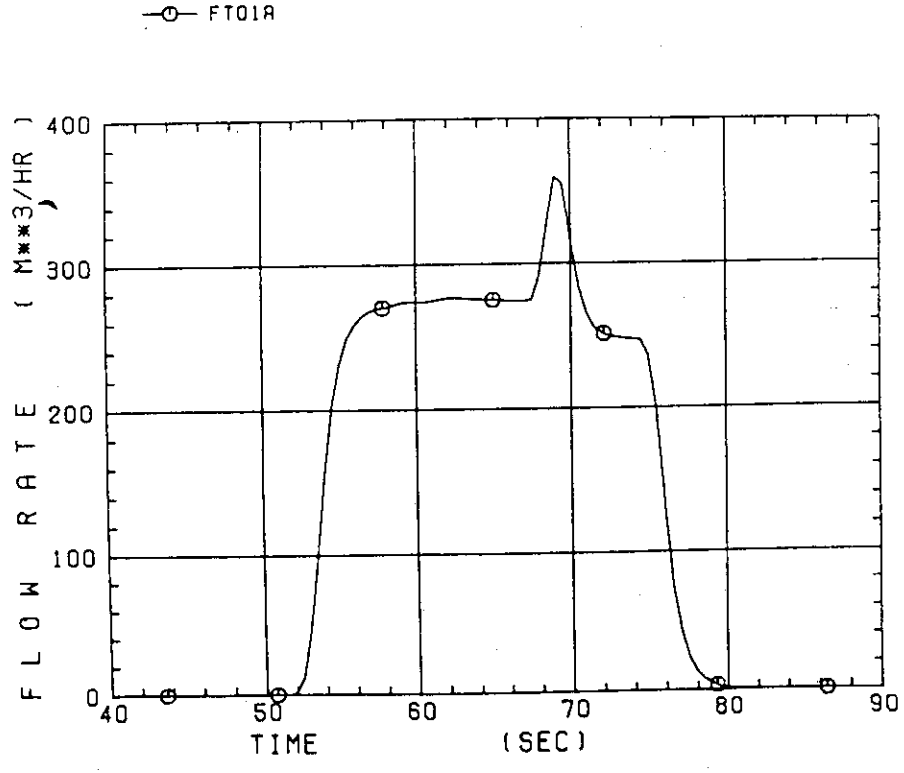

Fig. C-34 Total accumulator injection rate

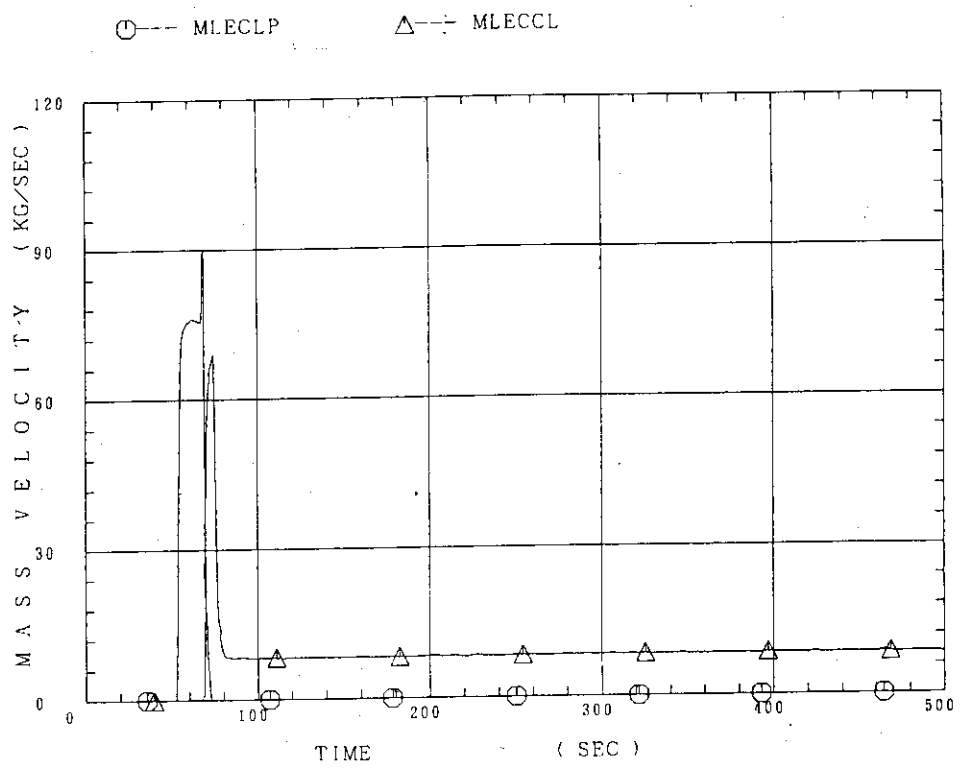

Fig. C-35 ECC water injection rates to lower plenum and to cold legs

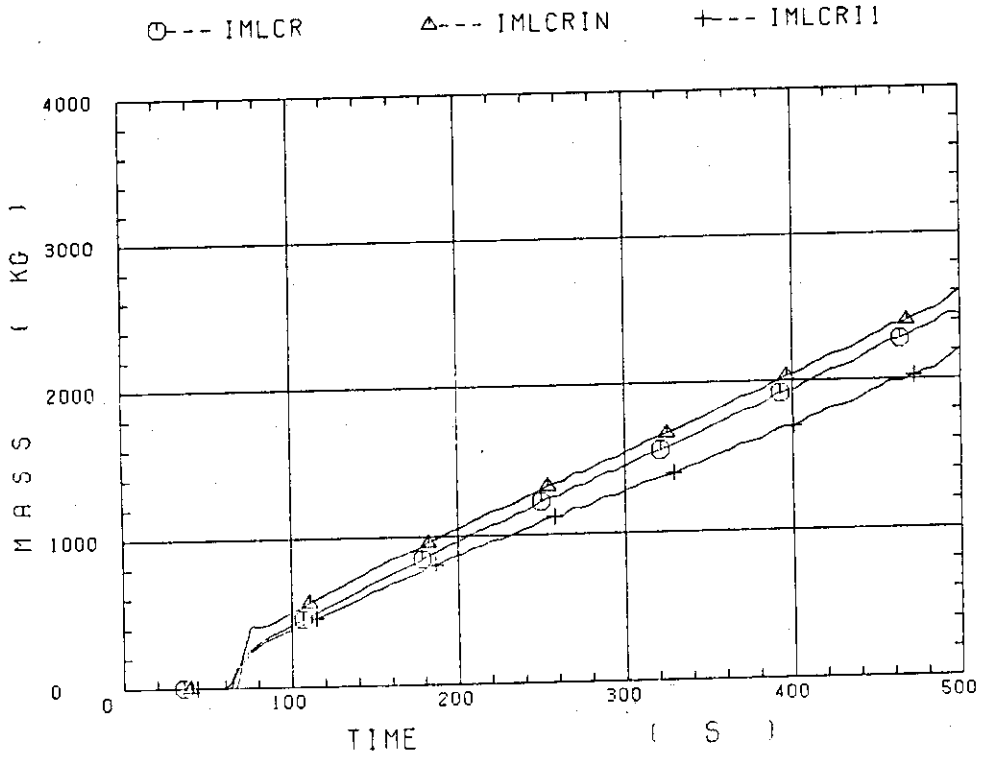

Fig. C-36 Integral core-flooded water masses evaluated with Eqs. (1) and (8) and the best-estimated